SMAC mimetics promote NIK-dependent inhibition of CD4+ TH17 cell differentiation

Rizk, John ; Kaplinsky, Joseph ; Agerholm, Rasmus ; Kadekar, Darshana ; Ivars, Fredrik ; Agace, William W ; Wong, W Wei-Lynn ; Szucs, Matthew J ; Myers, Samuel A ; Carr, Steven A ; Waisman, Ari ; Bekiaris, Vasileios

Abstract: Second mitochondria-derived activator of caspase (SMAC) mimetics (SMs) are selective antagonists of the inhibitor of apoptosis proteins (IAPs), which activate noncanonical NF- B signaling and promote tumor cell death. Through gene expression analysis, we found that treatment of CD4<jats:sup>+</jats:sup> T cells with SMs during T helper 17 (T<jats:sub>H</jats:sub>17) cell differentiation disrupted the balance between two antagonistic transcription factor modules. Moreover, proteomics analysis revealed that SMs altered the abundance of proteins associated with cell cycle, mitochondrial activity, and the balance between canonical and noncanonical NF- B signaling. Whereas SMs inhibited interleukin-17 (IL-17) production and ameliorated T<jats:sub>H</jats:sub>17 cell–driven inflammation, they stimulated IL-22 secretion. Mechanistically, SM-mediated activation of NF- B–inducing kinase (NIK) and the transcription factors RelB and p52 directly suppressed <jats:italic>Il17a</jats:italic> expression and IL-17A protein production, as well as the expression of a number of other immune genes. Induction of IL-22 production correlated with the NIK-dependent reduction in cMAF protein abundance and the enhanced activity of the aryl hydrocarbon receptor. Last, SMs also increased IL-9 and IL-13 production and, under competing conditions, favored the differentiation of naïve CD4<jats:sup>+</jats:sup> T cells into T<jats:sub>H</jats:sub>2 cells rather than T<jats:sub>H</jats:sub>17 cells. These results demonstrate that SMs shape the gene expression and protein profiles of T<jats:sub>H</jats:sub>17 cells and inhibit T<jats:sub>H</jats:sub>17 cell–driven autoimmunity.

DOI: https://doi.org/10.1126/scisignal.aaw3469

IMMUNOLOGY

SMAC mimetics promote NIK-dependent inhibition of CD4$^+$ T_H17 cell differentiation

John Rizk[1], Joseph Kaplinsky[1], Rasmus Agerholm[1], Darshana Kadekar[1], Fredrik Ivars[2], William W. Agace[1,2], W. Wei-Lynn Wong[3], Matthew J. Szucs[4], Samuel A. Myers[4], Steven A. Carr[4], Ari Waisman[5], Vasileios Bekiaris[1]*

Second mitochondria-derived activator of caspase (SMAC) mimetics (SMs) are selective antagonists of the inhibitor of apoptosis proteins (IAPs), which activate noncanonical NF-κB signaling and promote tumor cell death. Through gene expression analysis, we found that treatment of CD4$^+$ T cells with SMs during T helper 17 (T_H17) cell differentiation disrupted the balance between two antagonistic transcription factor modules. Moreover, proteomics analysis revealed that SMs altered the abundance of proteins associated with cell cycle, mitochondrial activity, and the balance between canonical and noncanonical NF-κB signaling. Whereas SMs inhibited interleukin-17 (IL-17) production and ameliorated T_H17 cell–driven inflammation, they stimulated IL-22 secretion. Mechanistically, SM-mediated activation of NF-κB–inducing kinase (NIK) and the transcription factors RelB and p52 directly suppressed *Il17a* expression and IL-17A protein production, as well as the expression of a number of other immune genes. Induction of IL-22 production correlated with the NIK-dependent reduction in cMAF protein abundance and the enhanced activity of the aryl hydrocarbon receptor. Last, SMs also increased IL-9 and IL-13 production and, under competing conditions, favored the differentiation of naïve CD4$^+$ T cells into T_H2 cells rather than T_H17 cells. These results demonstrate that SMs shape the gene expression and protein profiles of T_H17 cells and inhibit T_H17 cell–driven autoimmunity.

INTRODUCTION

CD4$^+$ T helper 17 (T_H17) cells are the major adaptive immune cell subset participating in type 3 immunity, which is characterized by production of the cytokines interleukin-17 (IL-17) and IL-22. This type of immune response occurs in response to extracellular bacteria and fungi (*1*, *2*) or during chronic inflammatory diseases (*3*), like multiple sclerosis and psoriasis (*4*). T_H17 cells themselves produce IL-17, IL-21, and IL-22 (*5*), and their differentiation program is under the control of a well-defined set of transcription factors (TFs) such as retinoic acid receptor (RAR)–related orphan receptor γt (RORγt), signal transducer and activator of transcription 3, cellular MAF (cMAF), and the heterodimeric complex of interferon regulatory factor 4 (IRF4) and basic leucine zipper ATF-like transcription factor (BATF) (*3*, *6*–*12*).

The nuclear factor kappa light-chain enhancer of activated B cells (NF-κB) pathway is a determinant of multiple fate decisions in T cells (*13*), and during priming, it can be initiated downstream of the T cell receptor (TCR), CD28, and costimulatory tumor necrosis factor (TNF) superfamily members (*14*). The NF-κB pathway is divided into the canonical and noncanonical branches depending on the mobilization of the TFs NFKB1 (p50), RelA (p65), and c-Rel or NFKB2 (p52) and RelB, respectively (*15*). Hence, the two NF-κB pathways can induce diverse gene signatures (*13*, *16*), and both have been implicated in T_H17 differentiation (*17*, *18*). Thus, whereas p65 and c-Rel are important in driving RORγt expression (*17*), RelB inhibits efficient RORγt binding to the *Il17a* promoter (*18*). In contrast, the noncanonical NF-κB pathway promotes development of T_H9 cells (*19*).

Cellular inhibitor of apoptosis protein–1 (cIAP1) and cIAP2 are E3 ubiquitin ligases that function to activate the canonical NF-κB pathway and inhibit the noncanonical NF-κB pathway (*20*). Downstream of TNF receptor 1 ligation, the presence of cIAP1/2 is important to initiate the canonical NF-κB pathway, whereas in their absence, cells may undergo programmed death (*21*, *22*). In contrast, cytoplasmic cIAP1/2 exists in a hetero-multimeric complex with TNF receptor–associated factor 2 (TRAF2), TRAF3, and NIK (NF-κB–inducing kinase) where it induces K48 ubiquitination of NIK leading to its continuous degradation (*23*–*25*). This pathway is used by various TNF superfamily receptors including TNFR2, CD40, and lymphotoxin β receptor (*26*). Thus, inhibition of cIAP1/2 leads to NIK stabilization and subsequent processing of p100 and nuclear translocation of p52 and RelB (noncanonical NF-κB). The mitochondrial protein SMAC targets and inhibits IAP family members, allowing caspase-mediated cell death (*27*, *28*).

SMAC mimetic (SM) compounds are small-molecule inhibitors that bind cIAP1/2 and promote their auto-ubiquitination and degradation or inactivation in the case of x-linked IAP (xIAP) (*29*, *30*). Treatment with SM leads to NIK protein stabilization and initiation of the noncanonical NF-κB pathway while, at the same time, sensitizing some cells to TNF-induced death (*29*–*31*). Because of their ability to induce cell death, different types of SM compounds, including mono- and bivalent, are currently in clinical trials against tumors as standalone (*32*, *33*) or in combination with checkpoint inhibitor treatments (*34*, *35*). Despite the clinical interest in SM, there is limited evidence of their impact on CD4$^+$ T cell biology. However, cIAP1/2 can enhance CD4$^+$ T cell activation (*36*, *37*), whereas SM treatment can kill HIV-infected CD4$^+$ T cells (*38*). Here, we showed that SM treatment of CD4$^+$ T cells has profound effects on their differentiation program and functionality. Our data provide molecular and mechanistic evidence that this activity of SMs was due to the activation of the noncanonical NF-κB pathway in this cell type.

[1]Department of Health Technology, Technical University of Denmark, Kemitorvet, Building 202, 2800 Kgs Lyngby, Denmark. [2]Department of Experimental Medical Science, Lund University, 22184 Lund, Sweden. [3]Institute of Experimental Immunology, University of Zurich, Winterthurerstrasse 190, Zurich, Switzerland. [4]Broad Institute of MIT and Harvard, Cambridge, MA 02142, USA. [5]Institute for Molecular Medicine, University Medical Center of the Johannes Gutenberg University of Mainz, Obere Zahlbacher Str. 67, Mainz 55131, Germany.
*Corresponding author. Email: vasbek@dtu.dk

RESULTS

Treatment with SM alters cytokine production by T_H17 cells

To address the role of SM treatment and cIAPs in T_H17 cells, we differentiated murine $CD4^+$ T cells into the T_H17 lineage in the presence of the SM AT-406 or dimethyl sulfoxide (DMSO) control. In this cell type, SM did not induce cell death (Fig. 1A), had no effect on early activation as measured by surface abundance of CD69 (fig. S1A), and did not affect proliferation (fig. S1, B and C). We confirmed that the concentration of SM that we were using effectively depleted cIAP1 from differentiating T cells but did not degrade xIAP (fig. S1D), as expected (*29*, *30*).

When we assessed the ability of T_H17 cells to produce IL-17 when differentiated in the presence of SM, we found that SM treatment inhibited IL-17A and IL-17F expression (Fig. 1, B to D). As expected (*29*, *30*), and in contrast to IL-17, SM treatment increased production of TNF protein but not its mRNA expression (fig. S2A). Increased TNF production in SM-treated cells was not responsible for the reduced amounts of IL-17A (fig. S2B). Despite the reduction in IL-17A, there was no alteration in the abundance of RORγt (fig. S3, A to C), IRF4, or BATF protein (fig. S3, D and E), despite the 0.6-fold decrease in mRNA expression of both *Irf4* and *Batf* (fig. S3, F and G). The effect on IL-17A was not specific to AT-406; it also occurred when cells were cultured with the SM LCL161 (fig. S4A). SM treatment additionally inhibited IL-17A production in human T_H17 cells (Fig. 1E). In agreement with redundancy between cIAP1 and cIAP2 (*39*), T cells lacking cIAP1, cIAP2, xIAP, or both cIAP2 and xIAP responded efficiently to SM (fig. S4B). Collectively, these data show that SM treatment of differentiating $CD4^+$ T cells does not affect cell death or proliferation; however, it blocks the expression of IL-17 by mouse and human T_H17 cells without affecting lineage commitment independently of individual cIAPs.

SM treatment exacerbates antagonistic TF expression in T_H17 cells

To get an unbiased view of the impact of SM treatment, we carried out microarray experiments (table S1A) from naïve $CD4^+$ T cells differentiated with or without SM for 48 hours under T_H17-polarizing conditions. SM substantially altered the transcriptional profile of T_H17 cells (fig. S6A), with the expression of 808 genes being decreased and the expression of 983 genes being increased significantly (Fig. 2A and table S1B). Using a twofold cutoff, we identified 100 differentially expressed genes, of which 36 were decreased and 64 were increased (Fig. 2A and table S1C). Of these genes, we identified nine that have known roles in either T_H17 differentiation or T_H17 function (*6*).

To understand how SM promote these gene expression differences in T_H17 cells, we clustered genes that were annotated in the validated KCRI network (*6*) as being important in T_H17 differentiation and function and were at the same time differentially expressed after SM treatment. This identified 41 genes, most of which were TFs that clustered into two antagonistic modules (Fig. 2, B and C). Module 1, which contained the key T_H17 TFs cMAF, aryl hydrocarbon receptor (AhR), IRF4, and BATF, acted as an enhancer to itself but as a suppressor to module 2 and was, in turn, suppressed by SM (Fig. 2C). In a similar manner, module 2, which contained NFKB2, REL, GATA3, and eomesodermin (EOMES) and was induced by SM, acted as an enhancer to itself but suppressed module 1 (Fig. 2C). This model supports the presence of antagonistic TF groups during T_H17 differentiation (*40*).

Our data indicated that SM treatment augmented the expression of a group of TFs that suppressed other key T_H17 TFs (Fig. 2C). Using a simple model to account for the fold changes that transcriptional activators and repressors impose on target genes, we compared the predicted fold change for all genes in the KCRI network with the measured fold change of the same genes in our experimental data. The majority of genes followed the same expression trend whether this was predicted or measured (e.g., the relatively large changes in *Il10*, *Il17a*, and *Nrp1* are well explained; Fig. 2D). However, there were a number of genes whose

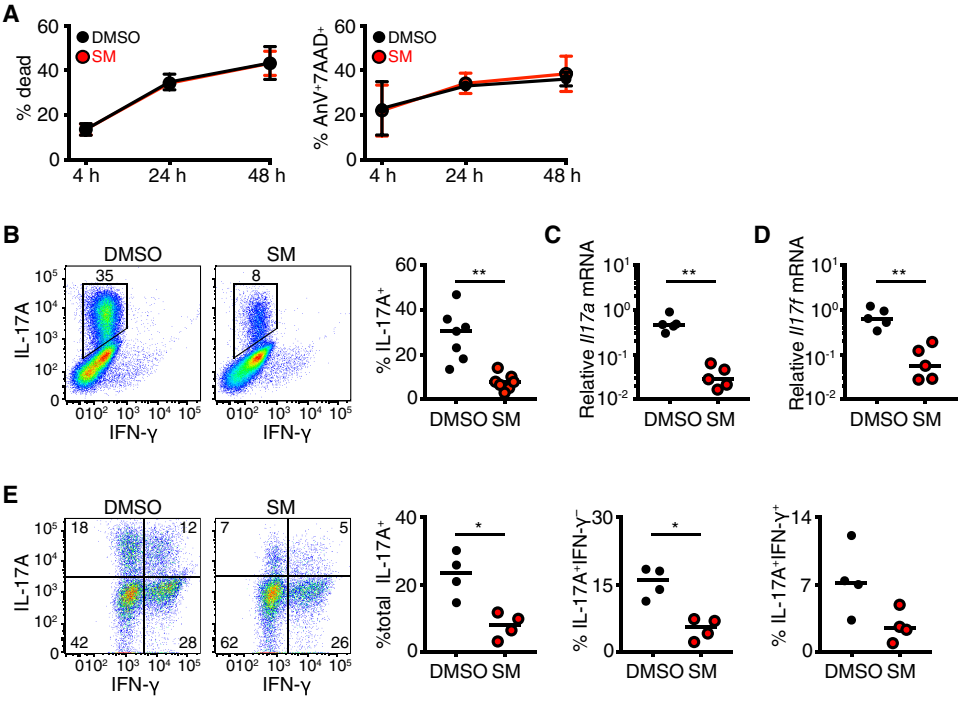

Fig. 1. Expression of IL-17 in mouse and human T_H17 cells after SM treatment. (**A**) Flow cytometry analysis of the viability of mouse T_H17 cells differentiated with DMSO control or SM AT-406 for the indicated times. Data are means ± SD pooled from three experiments. (**B**) Flow cytometry analysis of IL-17A and IFN-γ production by mouse T_H17 cells differentiated with DMSO or SM and treated for 48 hours. Dot plots (left) are representative of and quantified data with medians (right) are pooled from seven biological replicates. (**C** and **D**) Quantitative real-time PCR (qRT-PCR) analysis of *Il17a* and *Il17f* mRNA expression in mouse T_H17 cells differentiated with DMSO or SM for 48 hours. Data with medians are pooled from five biological replicates. (**E**) Flow cytometry analysis of IL-17A and IFN-γ production by live human $CD45RO^+RORγt^+$ T_H17 cells differentiated with DMSO or SM for 72 hours. Dot plots (left) are representative of and quantified data with medians (right) are pooled from four biological replicates. $^*P < 0.05$, $^{**}P < 0.01$ by Mann-Whitney test.

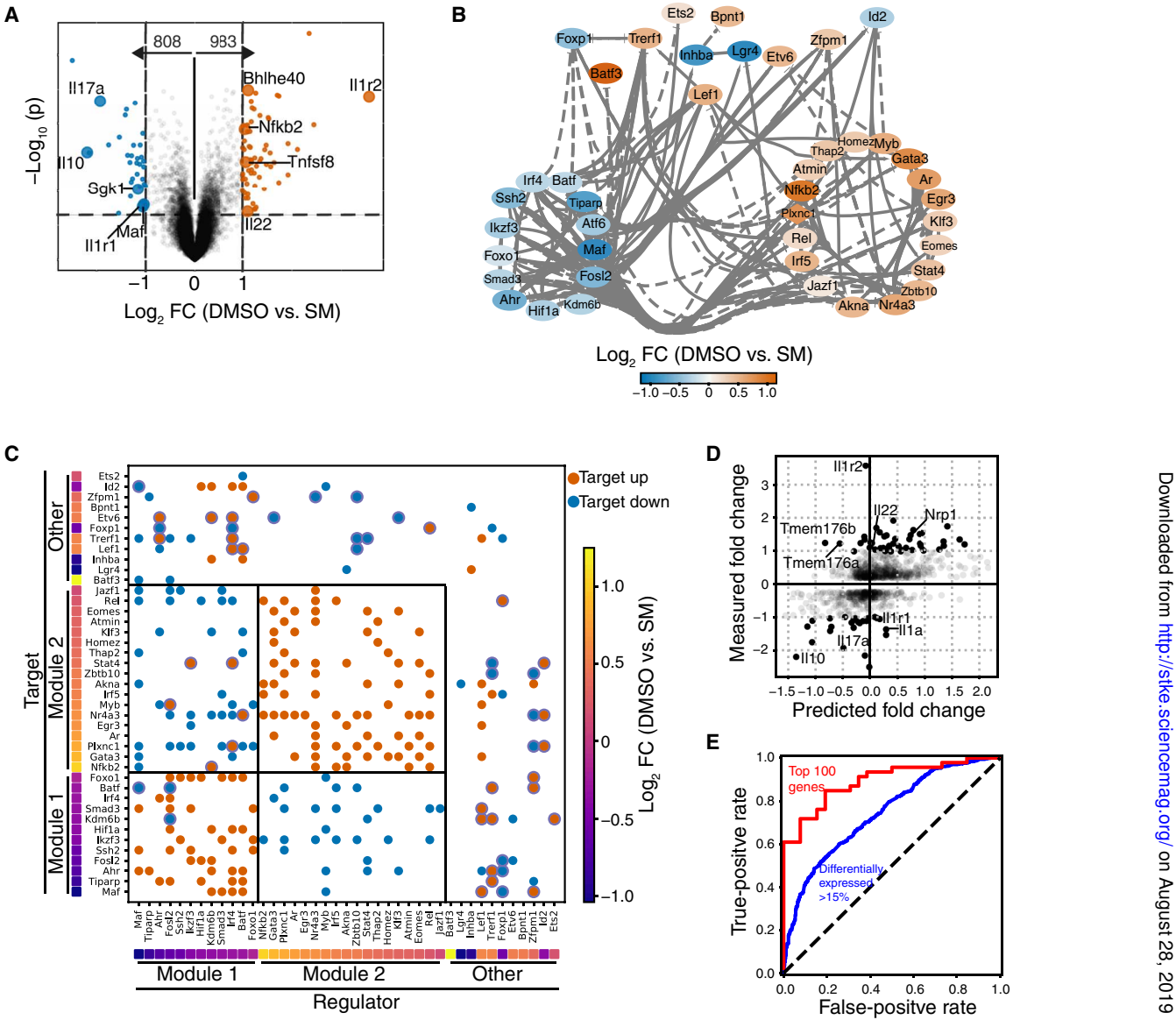

Fig. 2. SM induced transcriptional changes in T_H17 cells. (**A** to **C**) Microarray analysis of mouse T_H17 cells differentiated with DMSO or SM for 48 hours. Volcano plot of all differentially expressed genes after SM treatment (A) and network analysis of the differentially expressed genes annotated as regulators of downstream T_H17 targets (B), and regulatory interaction nodes (C) are from the analysis of five biological repeats. Positive (solid lines) and negative (dotted lines) regulation and differential expression after SM treatment are indicated. (**D** and **E**) Comparison of model predicting whether the gene expression changes (B and C) correspond to measured gene expression (D) and ROC curve testing the qualitative performance of the prediction model (E). FC, fold change. In (C) circled symbols indicate inconsistent target change.

expression pattern could not be explained by the simple transcriptional module model, which are likely to be important for T_H17 function (e.g., *Il1r1*, *Il1r2*, *Il1a*, *Il22*, *Tmem176a*, and *Tmem176b*; Fig. 2D). However, the receiver operating characteristic (ROC) curve analysis of true- and false-positive rate indicated that our two-module model was a very good classifier for the top 100 genes (Fig. 2E). This model also performed reasonably across the wider transcriptome of 1106 genes annotated in the KCRI network where differential expression was greater than 15% (Fig. 2E). Therefore, our model defining the existence of two opposing TF modules can be used confidently to explain many of the wider changes across the transcriptome that occur as a result of SM treatment.

SM increases the abundance of NF-κB signaling, adhesion, and cell cycle proteins in T_H17 cells

cIAP1/2 are E3 ligases that activate downstream signaling through ubiquitin-dependent protein turnover or through the formation of a signaling scaffold complex. Thus, much of their biological impact is independent of gene expression. Global proteomics analysis of $CD4^+$ T cells differentiated under T_H17 conditions for 24 or 48 hours revealed that SM altered the abundance of a number of proteins belonging to diverse structural and functional groups (fig. S6B and table S2, A and B). To identify the cellular processes these proteins were involved in and to understand the impact of SM on T_H17 biology, we used changes in protein abundance (table S2, C and D) to decipher

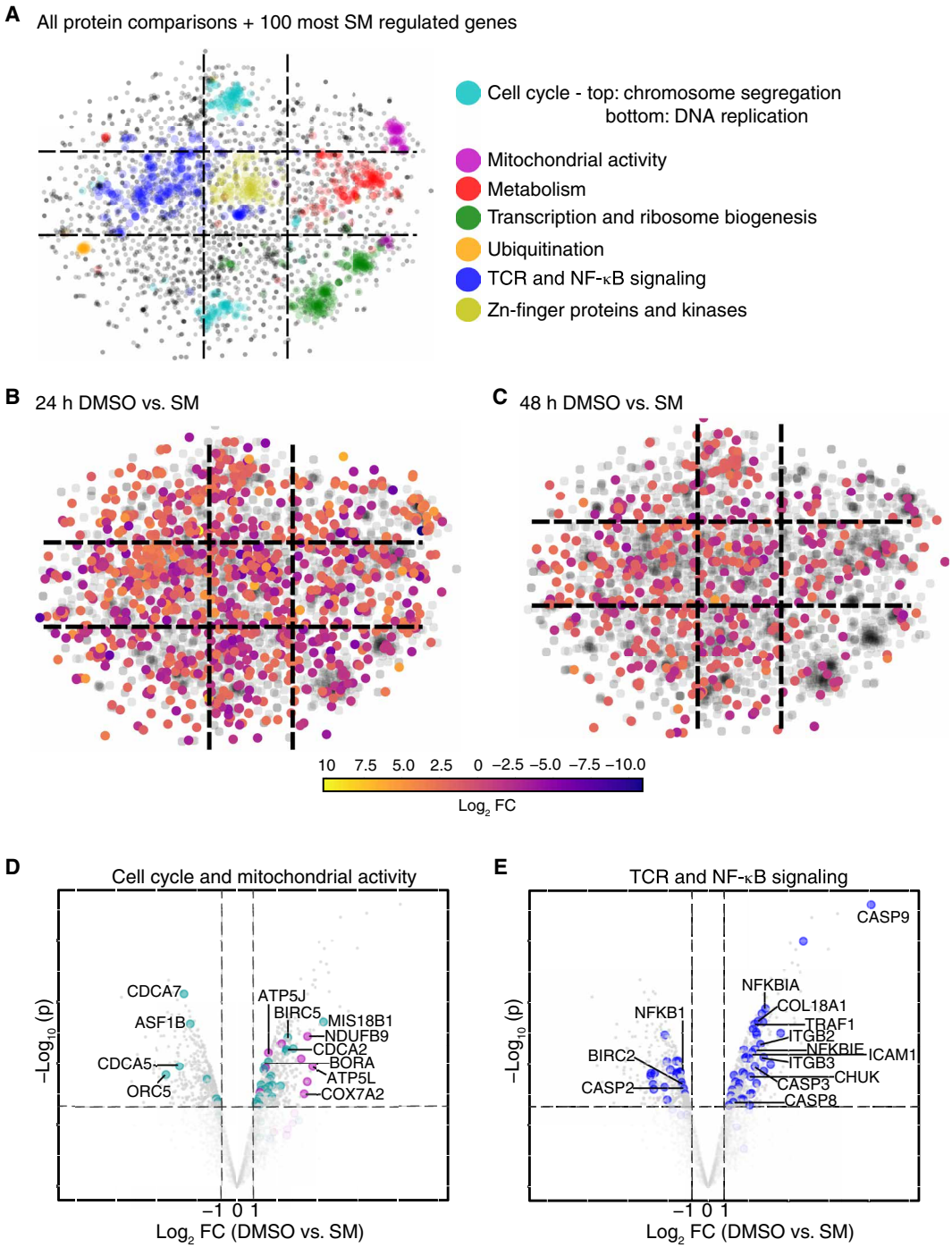

Fig. 3. SM induced proteomic changes in T_H17 cells. (**A** to **E**) Mass spectrometry analysis of mouse T_H17 cells differentiated with DMSO or SM for the indicated times. All twofold change protein changes across comparisons and 100 differentially expressed genes analyzed for functional similarity by tSNE analysis of STRING database annotations (A) are from two biological repeats. Proteins whose abundance changed from control by twofold or more in both replicates of SM-treated cells at 24 hours (B) or 48 hours (C) are colored by average fold change. Volcano plots indicate proteins with differential abundance in both biological replicates 24 hours after SM treatment within the TCR and NF-κB signaling cluster (D) or the cell cycle and mitochondrial activity clusters (E).

which pathways were present in differentiated T_H17 cells or after SM treatment. Within a set of all the proteins that were changed by greater than twofold between all comparisons (table S2) and the 100 differentially expressed genes after SM treatment, we used spectral clustering to identify functional clusters based on the annotation of these targets in the STRING database (Fig. 3A and fig. S5A). Such analysis resulted in the identification of seven clusters corresponding to the cellular processes of (i) cell cycle, (ii) mitochondrial activity, (iii) metabolism, (iv) transcription and ribosomal biogenesis, (v) ubiquitination, (vi) TCR and NF-κB signaling, and (vii) Zn-finger proteins and kinases (Fig. 3A). We then investigated in-depth how proteins within the enriched clusters changed with T_H17 differentiation and/or SM treatment. For this, we considered proteins that changed by twofold or more in both biological replicates (Fig. 3, B and C). To ensure that the clustering of changes that we observed was not random, we calculated how the correlation in protein abundance varied with distance on the t-distributed stochastic neighbor embedding (tSNE) graph, in each comparison; these were then compared to controls where the data were randomly permuted. Proteins that were clustered together showed significantly greater correlation in our data than in random permutations (fig. S6, C to F).

We noticed that, at 24 hours, activated $CD4^+$ T cells cultured under T_H17 conditions had increased transcriptional and ribosomal activity, as well as more abundant DNA replication proteins than their undifferentiated counterparts (fig. S5, B and D). Although glycolysis is important for T_H17 differentiation (*41*–*43*), in comparison to undifferentiated $CD4^+$ T cells, the abundance of many proteins involved in metabolic processes including glycolysis, fatty acid metabolism, and the tricarboxylic acid (TCA) cycle was reduced at 24 and 48 hours in T_H17 cells (figs. S5, B and E, and S7A, and table S3). However,

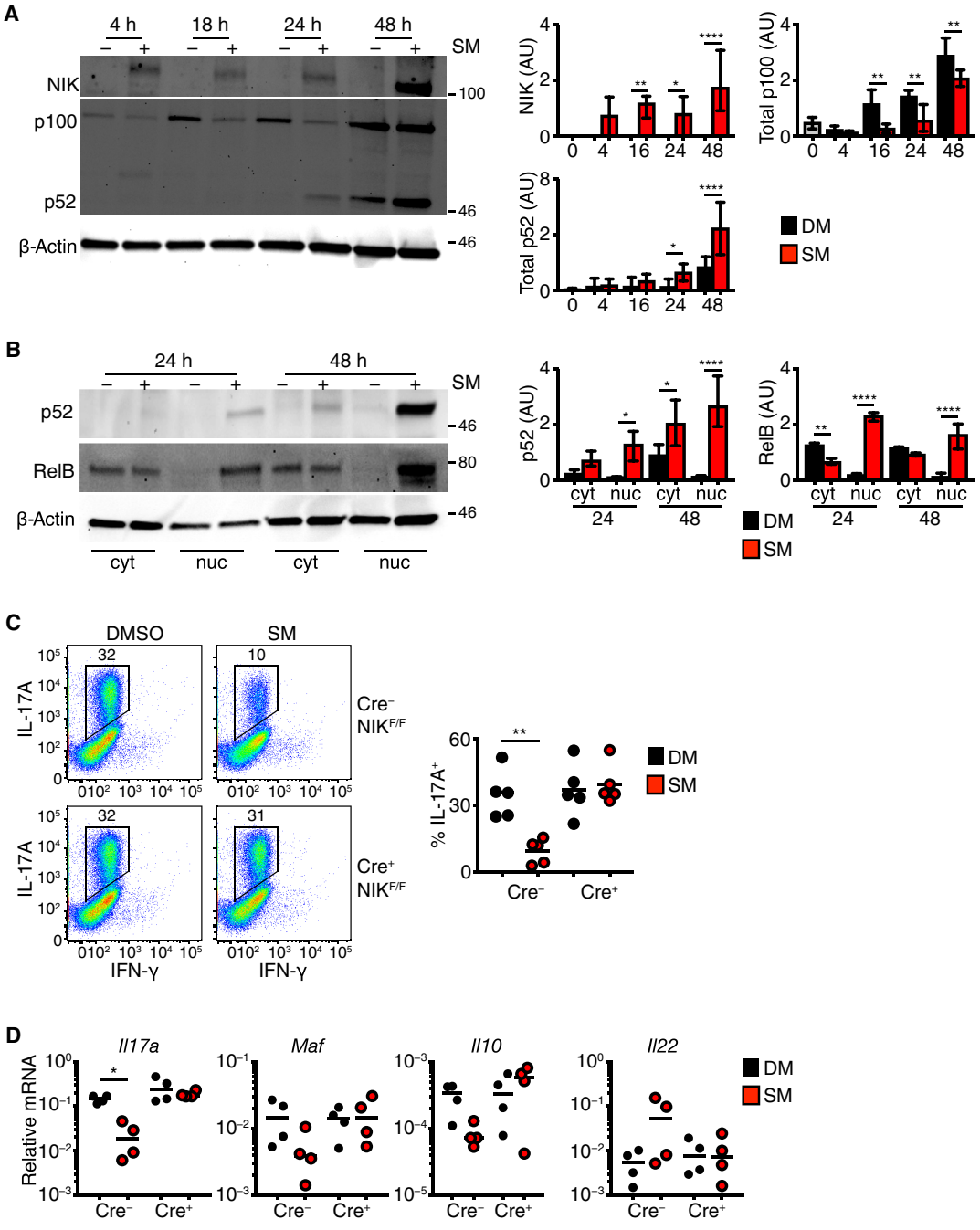

Fig. 4. SM drives NIK-dependent changes in T_H17 cells. (**A** and **B**) Western blot for NIK and p100/p52 (A) or p52 and RelB subcellular location (B) in lysates of mouse T_H17 cells treated with DMSO or SM for the indicated times. Blots (left) are representative of four experiments. Quantified band intensity values (right) are mean ± range pooled from all experiments. AU, arbitrary units. (**C**) Flow cytometry analysis of IL-17A and IFN-γ production by mouse $CD4^{CRE}$-$NIK^{F/F}$ or control (Cre^-) T_H17 cells treated with DMSO or SM for 48 hours. Dot plots (left) are representative of and quantified frequency data with medians (right) are pooled from five biological replicates. (**D**) qRT-PCR analysis of *Il17a*, *Maf*, *Il10*, and *Il22* mRNA expression in mouse $CD4^{CRE}$-$NIK^{F/F}$ or control (Cre^-) T_H17 cells treated with DMSO or SM for 48 hours. Data with medians are from four experiments. $^*P < 0.05$, $^{**}P < 0.01$, $^{****}P < 0.0001$ by Fisher's LSD ANOVA (A and B) or Mann-Whitney test (C and D).

our data were generated at early time points when the cells were not yet rapidly dividing. Overall, there was little difference between 24 and 48 hours with the exception of an increased abundance in proteins involved in chromosome segregation (fig. S5C).

Relative to DMSO controls, SM-treated T_H17 cells had increased amounts of proteins involved in chromosomal segregation and mitochondrial activity as well as proteins involved in metabolism, although this was not restricted to a specific pathway (Fig. 3, B to D, fig. S7B, and table S4). Furthermore, SM increased the abundance of inhibitors of canonical NF-κB signaling, such as NF-κB inhibitor α (IκBα) and IκBε, as well as the kinase IKKα (IκB kinase α) (fig. S8A). At the same time, SM reduced the abundance of NFKB1 itself (Fig. 3E and fig. S8A). Most of the changes associated with NF-κB and other pathways were transient and not distinctly present at 48 hours, with the exception of increased RelB abundance (table S4). In comparison to undifferentiated T cells, T_H17 cells had increased amounts of NFKB1 and decreased amounts of IκBα, IκBε, and IKKα (fig. S8B and table S3). These data suggest that normal T_H17 differentiation requires canonical NF-κB signaling, which is antagonized by SM-induced activation of the noncanonical NF-κB pathway. SM-treated cells were also enriched in proteins associated with cell adhesion (e.g., Icam1, Itgb1, Itgb2, Itgb3, and CD44) and extracellular matrix interactions (e.g., Col2a1, Col3a1, and Col18a1) (Fig. 3E, fig. S8A, and table S4). Thus, SM may also have the potential to influence cell-to-cell communication and migration and limit NF-κB activity.

SM-driven alterations in T_H17 function depend on the noncanonical NF-κB pathway

In addition to its impact on proteins involved in NF-κB signaling (Fig. 3B and fig. S8), SM significantly increased the expression of

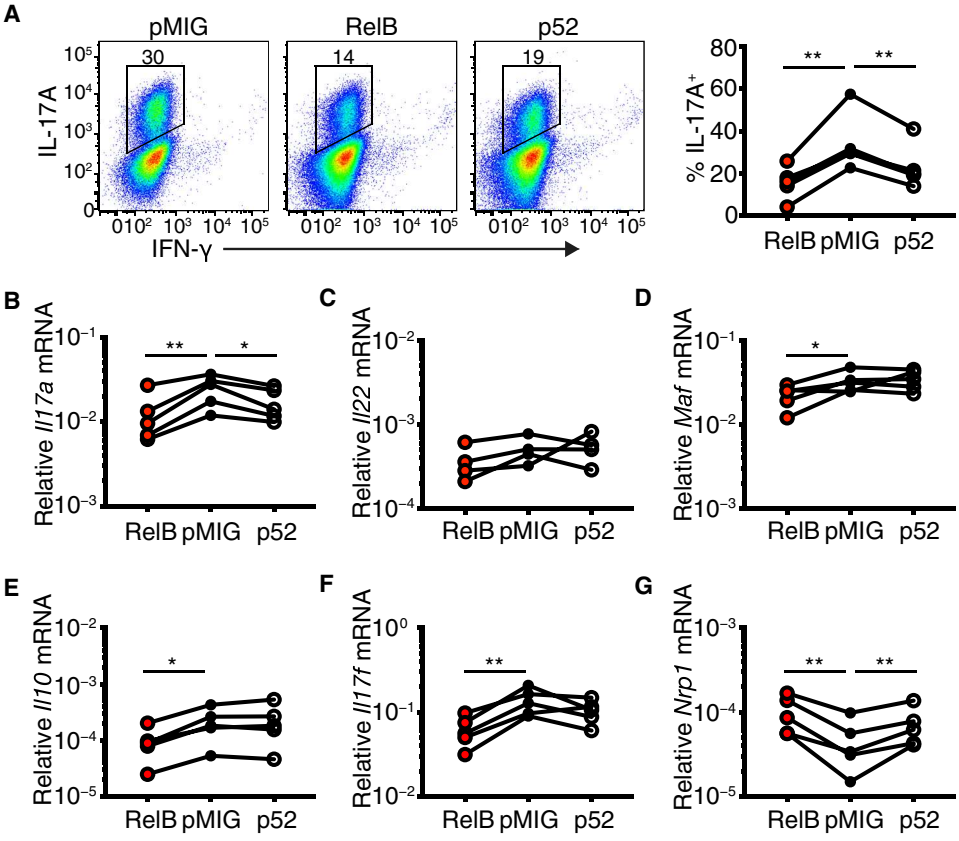

Fig. 5. Both RelB and p52 contribute to SM-associated changes in T_H17 cell gene expression. (**A**) Flow cytometry analysis of IL-17A and IFN-γ production by live, $CD69^+GFP^+$ mouse T_H17 cells transduced with the indicated retrovirus. Dot plots (left) are representative of and quantified data (right) are pooled from five independent experiments. (**B** to **G**) qRT-PCR analysis of *Il17a* (B), *Il22* (C), *Maf* (D), *Il10* (E), *Il17f* (F), and *Nrp1* (G) mRNA expression in FACS-sorted mouse GFP^+ T_H17 cells transduced with the indicated retrovirus. Data are pooled from five independent experiments. $^*P < 0.05$, $^{**}P < 0.01$ by paired *t* test.

Nfkb2 (Fig. 2A), which participated in multiple regulatory interactions (Fig. 2, B and C). We therefore reasoned that activation of the noncanonical NF-κB pathway by SM could partially explain the SM imprinted changes during T_H17 differentiation. Immunoblotting showed that SM treatment promoted stabilization of NIK and processing of p100 (Fig. 4A), as well as nuclear translocation of p52 and RelB (Fig. 4B and fig. S11). Because NIK is necessary to initiate p100 processing and the progress of the noncanonical NF-κB pathway, we assessed how SM affected T_H17 cells from mice where NIK was conditionally deleted using the Cre recombinase under the CD4 promoter ($CD4^{CRE}$-$NIK^{F/F}$). SM treatment failed to decrease IL-17A production in NIK-deficient cells (Fig. 4, C and D), indicating that the noncanonical NF-κB pathway is necessary for the impact of SM on T_H17 differentiation. Similar results were observed in *Il17a* mRNA expression (Fig. 4D) and additionally SM failed to increase TNF production (fig. S2C). Therefore, SM-induced noncanonical NF-κB activation is critical for regulating the differentiation potential of the T_H17 lineage.

The noncanonical NF-κB TFs RelB and p52 can act as both a heterodimer and a homodimer independent of each other (*44*, *45*). To test whether RelB or p52 could be responsible for affecting T_H17 differentiation, we ectopically expressed them in T_H17 cells using a pMSCV-IRES-GFP (pMIG) retroviral transduction system and assessed expression of IL-17A. Both RelB and p52, albeit milder, significantly reduced IL-17A expression (Fig. 5, A and B). Ectopic coexpression of RelB and p52 in T_H17 cells did not further affect IL-17A, indicating no synergy between them (fig. S9A), which could be due to the significant induction of *Nfkb2* expression after ectopic RelB expression (fig. S9B). Although neither RelB nor p52 influenced expression of *Il22* (Fig. 5C), overexpression of RelB reduced *Maf* expression (Fig. 5D). Similarly, expression of *Il10* and *Il17f* was reduced after only RelB overexpression (Fig. 5, E to G), whereas the expression of neuropilin-1 (*Nrp1*), one of the top SM-induced genes (table S1C), was increased by both RelB and p52 (Fig. 5H). Mechanistically, RelB interferes with the ability of RORγt to bind the *Il17a* promoter (*18*). We found that less RORγt bound the *Il17a* promoter and enhancer [conserved noncoding sequence 5 (CNS5)] regions in SM-treated cells than control cells (fig. S10A). We also measured RORγt binding at the *Btla* promoter, a repressive target of RORγt (*46*), (fig. S10B) and found increased amounts of B and T lymphocyte–associated (BTLA) protein after SM treatment (fig. S10, C and D). In addition to BTLA, SM increased the surface abundance of the related immune checkpoint inhibitors PD-1 and LAG3 (fig. S10, E to H). Collectively, our data suggest that SM inhibit T_H17 development by limiting NIK-dependent activation of the noncanonical NF-κB pathway through the combined action of the TFs RelB and p52.

SM alters transcriptional regulation of IL-22 production

Il22 and *Maf* were among the most differentially expressed genes in SM-treated T_H17 cells (Fig. 2A), and we found that RelB suppressed *Maf* (Fig. 5, C and D). We confirmed that SM increased the abundance of IL-22 and reduced that of cMAF protein (Fig. 6, A and C). Because cMAF is a suppressor of IL-22 (*47*), we tested whether cMAF reconstitution in SM-treated T_H17 cells could rescue IL-22 expression. When we infected T_H17 cells with an empty retrovirus, SM induced expression of *Il22* (Fig. 6B). However, in the presence of a cMAF-expressing retrovirus, SM did not increase the expression of *Il22* compared to DMSO-treated T_H17 cells (Fig. 6B). Production of IL-22 is mostly dependent on activation of the AhR (*48*); therefore, we hypothesized that SM may additionally affect AhR. Whereas treatment with the AhR inhibitor CH-223191 diminished the SM-induced production of IL-22, AhR ligand FICZ enhanced the SM-induced increased production of IL-22 (Fig. 6D). These data suggest that SM modulates the control of IL-22 expression by reducing the expression of its transcriptional repressor cMAF and augmenting the activity of its activator, the AhR.

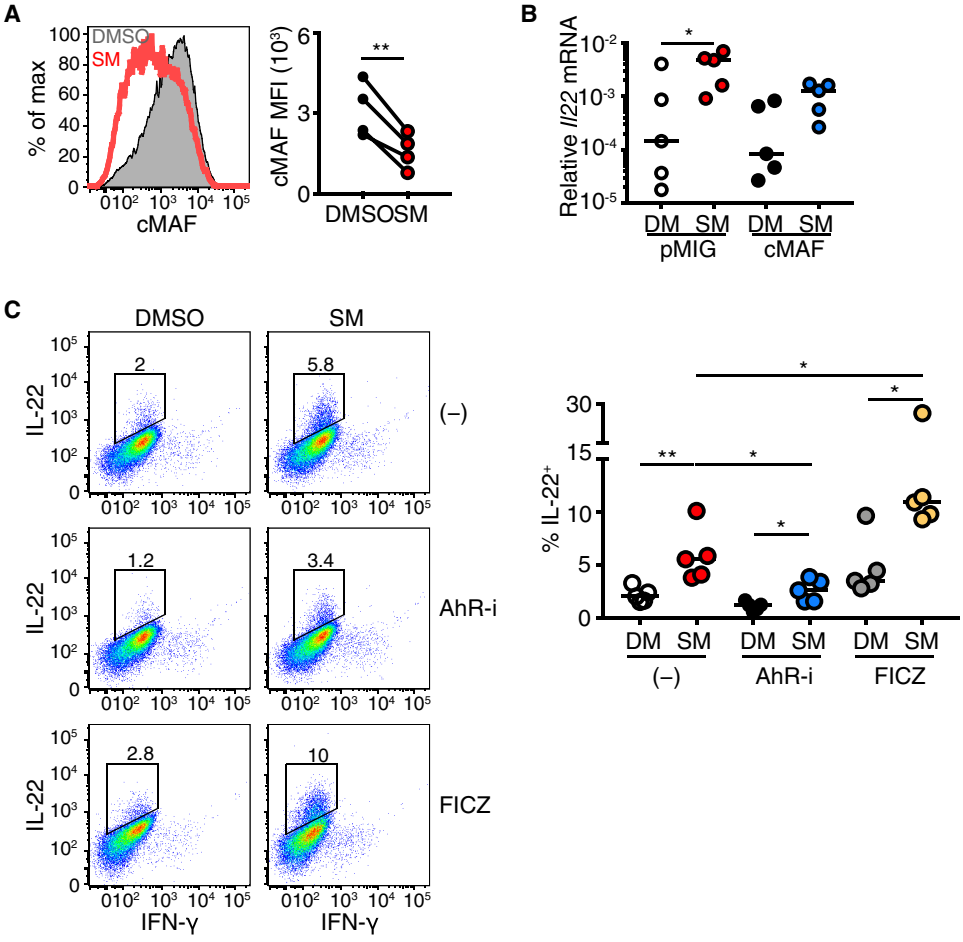

Fig. 6. SM augments AhR-dependent production of IL-22. (**A**) Flow cytometry analysis of cMAF abundance in T_H17 cells differentiated with DMSO or SM for 48 hours. Histograms (left) are representative of and quantified mean fluorescence intensity (MFI) data (right) are pooled from four biological replicates. (**B**) qRT-PCR analysis of *Il22* mRNA expression in FACS-sorted mouse GFP$^+$ T_H17 cells transduced with the indicated retrovirus. Data are pooled from five biological replicates. (**C**) Flow cytometry analysis of IL-22 and IFN-γ production by T_H17 cells differentiated with DMSO or SM and treated with AhR inhibitor (AhR-i) CH-223191 or FICZ, as indicated. Data with medians are from five biological replicates. *$P < 0.05$, **$P < 0.01$ by paired *t* test (A) or Mann-Whitney test (B and C).

SM treatment inhibits in vivo T_H17 function

To test the potential of SM to interfere with the in vivo differentiation of T_H17 cells in a type 3–driven disease, we treated mice that were immunized with myelin oligodendrocyte glycoprotein (MOG) to induce experimental autoimmune encephalomyelitis (EAE) (*49*) with SM. We found that three intraperitoneal injections of SM at days 0, 1, and 2, respectively, after immunization reduced IL-17A production by CD4$^+$ T cells in the spleen 1 week after immunization (Fig. 7A). We did not observe any difference in total activated CD44$^+$ CD4$^+$ T cell numbers between SM- and control-treated mice (Fig. 7A). These data suggested that the reduced frequency of IL-17A–producing cells was due to decreased IL-17A secretion, not due to defects in T cell activation or proliferation. Furthermore, we found that SM treatment reduced IL-17A production by gamma delta T (γδT17) cells but not their numbers (Fig. 7B). Thus, in vivo SM treatment has the potential to inhibit IL-17A production by both CD4$^+$ and γδ T cells.

Because of the importance of IL-17A in the development of EAE disease (*50*), we also analyzed whether SM treatment altered EAE disease progression in mice. Beginning 11 days after MOG immunization when symptoms of progressive paralysis usually occur, we observed less severe and delayed clinical symptoms in mice that received SM compared to control-treated mice (Fig. 7C). These data correlated with our earlier finding that SM reduced early IL-17A production by CD4$^+$ and γδ T cells. Collectively, our data show that SM have the potential to suppress T cell–associated IL-17A production during an inflammatory response, which may have implications in disease outcome.

SM promotes T_H2 and T_H9 differentiation at the expense of T_H17 and T_{regs}

Our observations that SM interfered with various pathways suggested that these compounds may have a broader impact on CD4$^+$ T cells and not just in the T_H17 subset. To test this, we differentiated murine CD4$^+$ T cells under T_H1, T_H2, T_H9, and regulatory T cell (T_{reg})–polarizing conditions in the presence of SM and assessed cytokine production 2 days later. We found that SM had no effect on interferon-γ (IFN-γ) production by T_H1 cells but induced a substantial increase in IL-13 and IL-9 by T_H2 and T_H9 cells (Fig. 8A). In marked contrast to inducing T_H2/T_H9 cells, SM-treated CD4$^+$ T cells cultured under T_{reg} skewing conditions expressed significantly less Foxp3 (Fig. 8A).

We also saw increased *Gata3* and *Il13* mRNA expression in SM-treated T_H17 cells when compared to wild-type cells (table S1B). This suggested that SM might interfere with the balance of T_H cell differentiation. To test this, we cultured CD4$^+$ T cells in the presence of IL-1β, IL-2, IL-4, IL-6, and transforming growth factor–β1 (TGF-β1) while blocking IFN-γ only. Under these competitive and unrestrictive conditions, which allow T cells to differentiate into all potential lineages besides T_H1, SM suppressed production of IL-17A and IL-10 while concomitantly inducing IL-9, IL-13, and TNF (Fig. 8B). These data indicate that SM treatment has the potential to influence the balance of T_H cell subsets. Thus, SM have potent context-dependent effects on the differentiation and function of most T_H subtypes, which may collectively limit the severity of autoimmunity.

DISCUSSION

We demonstrated that SM activated the noncanonical NF-κB pathway in a NIK-dependent manner and reprogrammed T_H17 cell differentiation and function. We showed that treatment with SM fundamentally changed the T_H17 transcriptome and proteome. More specifically, our data revealed that SM altered the balance of two antagonistic

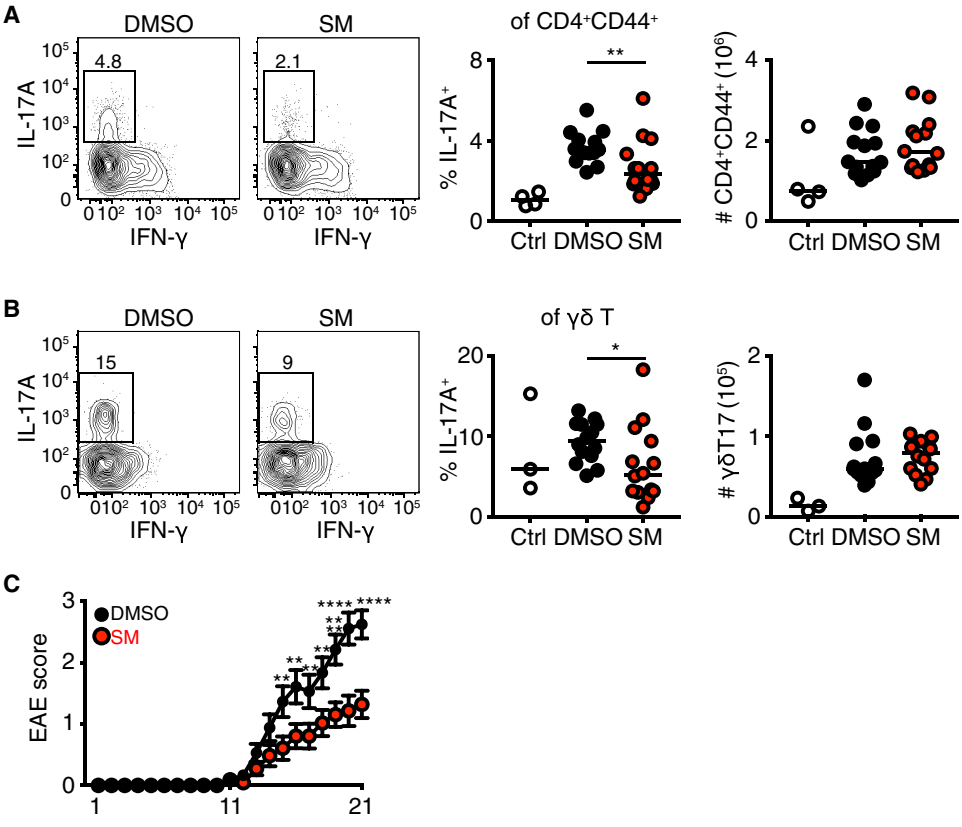

Fig. 7. SM reduces IL-17A production and limits EAE disease progression. (**A** and **B**) Flow cytometry analysis of IL-17A and IFN-γ production by splenic $CD44^+CD4^+$ T (A) and γδ T (B) cells from MOG-immunized mice treated with DMSO or SM after 7 days. Contour plots (left) are representative of four experiments. Quantified data with medians (right) are from all experiments. (**C**) Clinical scores from MOG-immunized mice treated as indicated. Data are means ± SEM of 27 mice from four experiments. $*P < 0.05$, $**P < 0.01$, $****P < 0.0001$ by Mann-Whitney test (A and B) or ANOVA with Bonferroni's multiple comparisons test (C).

transcriptional modules important for maintaining normal T_H17 physiology. At the proteome level, we found that SM switched on and off a number of key cellular processes in T_H17 cells and tipped the balance between canonical and noncanonical NF-κB. In vivo, SM had a mild but consistent inhibitory effect on IL-17A production and limited the development of autoimmune inflammation. Last, we found that treatment with SM boosted T_H2/T_H9 differentiation and skewed the balance between type 2 (e.g., T_H2) and type 3 (e.g., T_H17) $CD4^+$ T cells.

The T_H17 differentiation program is under strict transcriptional control by a number of important factors and pathways that work in synergy or sequentially to imprint the T_H17 phenotype (*6*, *40*). SM reorganized this transcriptional program by generating two opposing regulatory groups whereby TFs within a group reinforced each other and suppressed the opposing group. We suggest that TF coregulation and codependency is a common mechanism during T cell differentiation and that there are likely multiple transcriptional modules that positively or negatively regulate each other to establish a balanced gene expression profile.

Despite the plethora of data on the transcriptional programs of T_H17 and other T_H lineages, there is limited information on their global proteome changes during differentiation (*51*). Our data showed that some of the most substantial protein changes in differentiating T_H17 cells reflect a number of basic biological functions (e.g., metabolism, mitochondrial activity, and cell cycle). Compared to undifferentiated $CD4^+$ T cells, T_H17 cells showed reduced abundance of many proteins involved in energy-related pathways such as glycolysis, TCA, and fatty acid metabolism. Whether different T_H lineages show distinct protein profiles with regard to the above basic cellular functions is currently unknown but under investigation. Nevertheless, determining such global characteristic protein profiles will help not only to identify new targets for therapy or cell fate experimental manipulation but also to more accurately define the immunological component of inflammatory or infectious diseases.

Our experiments identified the unequivocal importance of the noncanonical NF-κB pathway in relaying many of the effects SM induced in T_H17 cells. Although the canonical NF-κB pathway affects all T cell subsets (*14*), the activation of the noncanonical NF-κB pathway will eventually determine the outcome of their differentiation program. Thus, whereas the noncanonical NF-κB pathway is required for type 2 responses (*19*), it suppresses T_H17 and T_{reg} differentiation (*18*, *52*). Here, we additionally show that favoring the noncanonical pathway with SM skews nondifferentiated T cells to become more T_H2-like and less T_H17-like, suggesting the possibility of manipulating in vivo T_H2-T_H17 balance with small-molecule IAP antagonists.

The increased incidence of allergy and autoimmune inflammation in Western Europe and the United States correlates with a misbalance of type 2 (T_H2) and type 3 (T_H17) immune responses (*53*, *54*). Type 2 responses dominate in allergies (such as allergic asthma), whereas type 3 responses dominate in most other autoinflammatory diseases (such as multiple sclerosis or psoriasis). Although T_H17 cells can suppress allergic responses (*54*), T_H2 cells suppress type 3 inflammation (*55*). In contrast, normal physiology requires a state of immune equilibrium where the different arms of the adaptive immune system are balanced (*56*). Therefore, the use of therapeutics to tip the T_H2-T_H17 balance will be beneficial for treating allergy or inflammation. We propose that antagonism of cIAP1/2 with SM compounds could provide a strategy to suppress T_H17 cells in vivo and instead promote T_H2 immunity. In contrast, manipulation of the TRAF2/3-cIAP1/2-NIK complex that controls noncanonical NF-κB activation, for instance, through NIK inhibition (*57*), could provide a mechanism whereby T_H2 cells are inhibited in allergic reactions.

SM compounds are currently in clinical trials as anticancer therapeutics and have been shown to have antitumor efficiency either alone (*32*, *33*) or in combination with immune checkpoint inhibitors (*34*, *35*). However, the molecular mechanisms by which they affect the immune system are largely unknown. The data we present herein

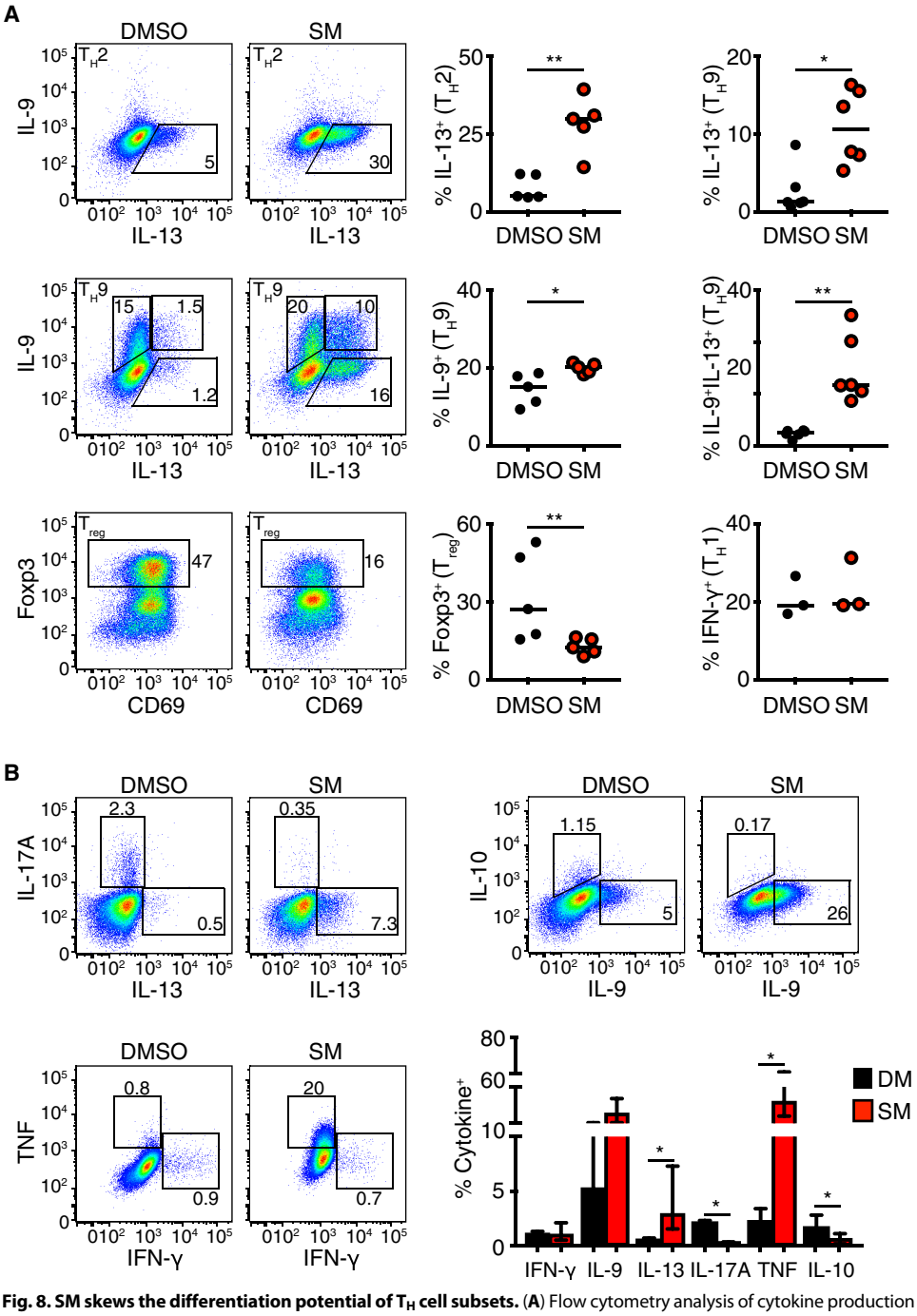

Fig. 8. SM skews the differentiation potential of T_H cell subsets. (**A**) Flow cytometry analysis of cytokine production by splenic $CD4^+$ T cells differentiated under the indicated T_H conditions in the presence of DMSO or SM for 48 hours. Dot plots (left) are representative of and quantified data with medians (right) are pooled from at least three biological replicates. (**B**) Flow cytometry analysis of cytokine production by splenic $CD4^+$ T cells were cultured under competitive conditions with IL-1β, IL-2, IL-4, IL-6, TGFβ1, and anti–IFN-γ for 48 hours. Dot plots (top left) are representative of four biological replicates. Quantified frequency data (right) are medians ± range pooled from all experiments. *$P < 0.05$, **$P < 0.01$ by Mann-Whitney test.

define the molecular and functional imprinting of SM treatment in $CD4^+$ T cells at the transcriptional and proteomic levels. Collectively, we show that SM treatment has a profound effect on T_H17 differentiation and physiology, as well as T_H17-driven disease, which suggest the potential use of SM drugs to alter the T_H2-T_H17 immune equilibrium.

MATERIALS AND METHODS

Mice

All animal breeding and experiments were performed in-house and only after approval from the Danish Animal Experiments Inspectorate. Mice deficient in IAPs were bred and maintained at the University of Zurich, Switzerland, and were used after permission from J. Silke (Victoria, Australia) (*58*). $CD4^{CRE}$-$NIK^{F/F}$ were bred and maintained at the University of Mainz, Germany (*59*). C57BL/6 mice were initially purchased from Taconic and bred in-house for all subsequent experiments. RORγt-GFP reporter mice (*60*) were generously provided by G. Eberl and subsequently bred in-house.

Cell culture media and buffers

Primary murine $CD4^+$ T cells were cultured in RPMI 1640 (Invitrogen) supplemented with 10% heat-inactivated fetal bovine serum (FBS; Gibco), 20 mM Hepes (Gibco) (pH 7.4), 50 μM 2-mercaptoethanol, 2 mM L-glutamine (Gibco), and penicillin-streptomycin (10,000 U/ml; Gibco). Iscove's modified Dulbecco's medium (IMDM) (Sigma) was used instead of RPMI 1640 when IL-22 measurement was required. The PlatE cell line was cultured in Dulbecco's modified Eagle's medium–GlutaMAX (Invitrogen) supplemented with 10% FBS and penicillin-streptomycin (10,000 U/ml). Fluorescence-activated cell sorting (FACS) buffer was prepared by mixing 3% heat-inactivated FBS with Dulbecco's phosphate-buffered saline (Gibco). FICZ [6-formylindolo(3,2b)carbazole] and CH-223191 (Sigma) were used at 300 nM and 3 μM, respectively.

In vitro differentiation of murine T_H2, T_H9, T_H17, and T_{reg}

Total $CD4^+$ T cells were isolated from mouse spleens using the EasySep Mouse $CD4^+$ T Cell Isolation Kit (STEMCELL Technologies). Purified $CD4^+$ T cells were then cultured in tissue culture plates coated with anti-CD3 (5 μg/ml; clone 145-2C11). Unless otherwise indicated, cells were cultured at 1.35×10^6 cells per well in 24-well plates, and anti-CD28 (2 μg/ml; clone 37.51) was added to all cultures. T_H1 cells were differentiated using anti–IL-4 (10 μg/ml; clone 11B11), hIL-2 (10 ng/ml), and IL-12 (10 ng/ml). T_H2 cells were differentiated using anti–IFN-γ (10 μg/ml; clone R4-6A2), hIL-2 (20 ng/ml), and IL-4 (50 ng/ml), whereas for T_H9 cells, anti–IFN-γ (10 μg/ml) was used together with hTGFβ1 (10 ng/ml), hIL-2 (20 ng/ml), and

IL-4 (250 ng/ml). T_H17 cells were differentiated using anti–IFN-γ (10 μg/ml), anti–IL-4 (10 μg/ml), anti-CD25 (5 μg/ml; clone PC61), and anti-CD122 (4 μg/ml; clone TM-β1) antibodies, hTGFβ1 (2 ng/ml), IL-6 (20 ng/ml), and IL-1β (10 ng/ml). For T_{regs}, antibody (10 μg/ml) against IFN-γ was used together with hTGFβ1 (5 ng/ml) and IL-2 (5 ng/ml). In cytokine competition experiments (Fig. 8B), cytokines used were IL-2 (20 ng/ml), IL-4 (50 ng/ml), TGFβ1 (2 ng/ml), IL-6 (20 ng/ml), and IL-1β (10 ng/ml). SMs AT-406 (Selleckchem) at 10 μM, LCL161 (Selleckchem) at 1 μM, or DMSO control was added to the cultures directly after addition of polarizing cytokines and antibodies.

In vitro culture of human T_H17 cells

All healthy donor material was collected from the central blood bank (Rigshospitalet, Copenhagen) under approval by the local Scientific Ethics Committee, and written informed consent was obtained according to the Declaration of Helsinki. Peripheral blood mononuclear cells (PBMCs) were isolated from whole blood by density centrifugation on Lymphoprep (Axis-Shield PoC) and cryopreserved at −150°C in FBS (Gibco) with 10% DMSO.

Total human $CD4^+$ T cells were isolated PBMC fractions using the EasySep Human $CD4^+$ T Cell Isolation Kit from STEMCELL Technologies. IMDM supplemented with 10% FBS (Gibco), 20 mM Hepes (pH 7.4) (Gibco), 50 μM 2-mercaptoethanol, 2 mM L-glutamine (Gibco), and penicillin-streptomycin (10,000 U/ ml; Gibco) was used for all cultures of human $CD4^+$ T cells. Purified human $CD4^+$ T cells were cultured in tissue culture plates coated with anti-hCD3 (1 μg/ml; clone OKT-3) at 1.5×10^6 cells per well in 24-well plates and anti-hCD28 (2.5 μg/ml; clone CD28.2), hIL-6 (30 ng/ml), hIL-1β (10 ng/ml), hTGFβ1 (0.5 ng/ml), and hIL-23 (10 ng/ml) were added. SM AT-406 (Selleckchem) at 10 μM or DMSO control was added to the cultures directly after addition of polarizing cytokines and antibodies.

Molecular cloning and construction of retroviral vectors

The complementary DNA (cDNA) for p52 and that for RelB were amplified from p52-cFLAG-pcDNA3 and RelB-cFLAG-pcDNA3, respectively, and were a gift from S. Smale (Addgene plasmid #20019 and #20017, respectively). The amplified RelB cDNA that was flanked by Eco RI and Xho I sites was subsequently cloned into pMIGII (Addgene plasmid #52107, a gift from D. Vignali) and pMIDsRed II (Addgene plasmid #52110, a gift from D. Vignali) using the same sites. The amplified p52 cDNA that was flanked by Sna BI site was subsequently cloned into pMIGII using the same sites. Plasmid sequences were validated by Sanger sequencing. pMIG-cMAF was a gift from C. C. Neumann (*61*). The retrovirus packaging cell line PlatE (Cell Biolabs) was transfected with the retrovirus encoding plasmids using FuGENE HD (Promega). The supernatant containing retrovirus particles was harvested 48 hours later and concentrated 100-fold by centrifugation at 50,000*g* for 90 min at 4°C. Virus aliquots were stored at −80°C until usage. Primers used to amplify p52 (containing restriction sites) were TATGTATACGTAATGGACAATTGCTACGATCCAG (forward) and ATGTTATACGTATTACTTGTCATCGTCGTCCTTGTAG (reverse). Primers used to amplify RelB (containing restriction sites) were TATGTAGAATTCATGCCGAGTCGCCGCG (forward) and ATGTTACTCGAGTTACTTGTCATCGTCGTCCTTGTAGTCG (reverse).

Infection of $CD4^+$ T cells with retroviral vectors

Total $CD4^+$ T cells were cultured at 10^6 cells per well for 16 to 18 hours with plate-bound anti-CD3 (5 μg/ml) and soluble anti-CD28 (2 μg/ml) antibodies. Subsequently, 15 μl of retroviral concentrate was added together with 2 μg of RetroNectin (Takara) to each well, followed by centrifugation at 700*g* at 32°C for 30 min without deceleration. After centrifugation, cells were incubated at 32°C for 90 min. Polarizing cytokines, antibodies, or DMSO and SMs were then added, and the cells were incubated for 48 hours at 37°C.

Flow cytometry staining

For intracellular cytokine staining, cells were treated with ionomycin (750 ng/ml; Sigma), phorbol myristate acetate (50 ng/ml; Sigma), and BD GolgiStop (1 μl/ml; containing monensin) for 3.5 hours before harvesting. For IL-22 analysis and for cytokine analysis of cultured human $CD4^+$ T cells, BD GolgiPlug (1 μl/ml; containing Brefeldin A) was used instead of BD GolgiStop. Cells were harvested by centrifugation at 400*g* for 5 min at 4°C, followed by staining with fixable viability stain (BD Horizon FVS700) for 10 min on ice in PBS. Subsequently, surface antigens were stained in FACS buffer for 30 min on ice. Mouse cells were fixed and permeabilized by incubation in BD fixation/permeabilization solution for 15 min at room temperature, followed by washing once in BD Perm/Wash solution. Intracellular cytokines were stained in BD Perm/Wash for 15 min at room temperature. For human cells and for TF staining in mouse cells, the cells were fixed using the fixation/permeabilization buffer in an eBioscience Foxp3 staining kit for 1 hour at 4°C. Cytokines were stained in permeabilization buffer from the same kit for 1 hour at 4°C. Antibodies used for flow cytometry were used at 1:200 dilution, unless otherwise specified. The following antibodies and fluorochromes were used herein: anti–IL-17A (TC11-18H10; BV786 and PE), anti–IFN-γ (XMG1.2; PE-Cy7 and APC), anti-TNF [MP6-XT22; BV650 and fluorescein isothiocyanate (FITC)], anti–IL-22 (1H8PWSR; PE), anti–IL-9 (D9302C12; PE), anti–IL-13 (Ebio13A; PE-Cy7), anti-CD69 (H1.2F3; V450 and Pe-CF594), anti-Foxp3 (FJK-16S; APC), anti-cMAF (symOF1; PE; 5 μl per test), anti-CD103 (M290; BV786), anti-CD4 (GK1.5; BUV395), anti-TCRγδ (GL3; BV421), anti-CD27 (LG.3A10; PE-Cy7), anti-CCR6 (140706; Alexa Fluor 647), anti-CD44 (1 M7; V500), anti-CD19 (6D5; FITC), anti-TCRβ (H57-597; APC-eflour780), anti-Ki67 (B56; BV786; 1:100), anti-IRF4 (3E4; PE), anti-hCD4 (RPA-T4; BB515; 1:25), anti-hCD45RA (HI100; BV605; 1:100), anti-hCD45RO (UCHL1; APC-H7; 1:50), anti-hIL17a (N49-653; BV650; 1:100), anti-hRORγt (AFKJS-9; PE), and anti–hIFN-γ (B27; BV480).

For cell cycle analysis, cells were fixed, after live dead exclusion and surface antigen staining, using the fixation/permeabilization buffer in the eBioscience Foxp3 staining kit for 1 hour at 4°C. Ki67 was stained in permeabilization buffer from the same kit for 1 hour at 4°C. Cells were washed once with permeabilization buffer, and the DNA content was stained using 5 μl of 7-aminoactinomycin D (7-AAD) per test for 10 min on ice in the same permeabilization buffer. Subsequently, FACS buffer was added to the samples and acquired immediately. Apoptosis was measured by staining cells with the Apoptosis Detection Kit (BD) using 5 μl of annexin V–PE and 5 μl of 7-AAD per test and following the manufacturer's protocol.

Western blotting

Cells were harvested, washed twice in ice-cold PBS, and subsequently resuspended in lysis buffer composed of 10 mM Tris-HCl (pH 7.5), 150 mM NaCl, and 0.5% TERGITOL (Sigma) supplemented with 1× protease inhibitor cocktail (Roche #4693159001). Cells were lysed by incubation for 45 min at 4°C in lysis buffer with rotation, followed

by 2 sonication cycles for 15 s on ice. Lysates were cleared by centrifugation at 12,000 rpm for 10 min at 4°C. Nuclear and cytoplasmic fractions were prepared using the NE-PER kit from Thermo Fisher Scientific according to the manufacturer's instructions. Precast SDS–polyacrylamide gel electrophoresis from Bio-Rad was loaded with about 20 μg of protein lysate per well. Proteins were subsequently wet-blotted on polyvinylidene difluoride membranes and then blocked in 5% nonfat dry milk in PBST (PBS with 0.5% Tween 20) for 1 hour at room temperature. Blocked membranes were probed with primary antibodies overnight at 4°C with shaking in 5% milk in PBST. Membranes were subsequently incubated with secondary antibodies for 1 hour at room temperature. The following primary antibodies used were purchased from Santa Cruz Biotechnology and used at 1:200 dilution: anti-Nfkb2 (c-5; SC-7386), anti-RelB (D-4; SC-48366), anti-IRF4 (M-17, SC-6059), and anti-BATF (WW8; SC-100974). Anti-RORγT (Q31-378) for Western blotting was purchased from BD and used at 1:1000 dilution. Anti-xIAP (2F1) and anti-cIAP1 (1E1-1-10) were purchased from ENZO and used at 1:500 dilution. Anti-NIK (#4994s) was purchased from CST and used at 1:500 dilution. Secondary horseradish peroxidase–linked antibodies used herein were as follows: anti-rabbit (CST #7074; 1:1000 dilution), anti-mouse (Santa Cruz #SC-2954; 1:2000 dilution), anti-goat (Santa Cruz #SC-2020; 1:2000 dilution), and anti-rat (ENZO #ADI-SAB-200-J; 1:5000 dilution).

The National Institutes of Health ImageJ software was used for densitometry analysis. Briefly, the signal intensity of protein bands was extracted using the "Analyze Gels" function. For each blot, the extracted intensities were then normalized across all intensities of the same band extracted from the same blot (band X normalized intensity $= \frac{\text{band } X \text{ intensity}}{\sum \text{intensities from all bands of the same protein}} \times 100$). Such normalized intensities were corrected against the normalized intensities of loading control (band X normalized ratio $= \frac{\text{band } X \text{ normalized intensity}}{\text{loading control normalized intensity}}$); the normalized ratios were expressed using the arbitrary units. For nuclear and cytoplasmic fractionation blots, the nuclear and cytoplasmic fractions were measured independently of each other.

RNA extraction, cDNA synthesis, and real-time PCR

Cells were lysed in RLT buffer (Qiagen) supplemented with 2-mercaptoethanol. Total RNA was extracted using an RNeasy mini kit (Qiagen) and then used for cDNA synthesis using an iScript cDNA synthesis kit (Bio-Rad), according to the manufacturer's protocol. SsoFast EvaGreen Supermix (Bio-Rad) was used to catalyze real-time polymerase chain reaction (PCR) reactions, which were run on CFX96 (Bio-Rad) and analyzed using Bio-Rad CFX manager software. Gene expression levels were normalized to that of β-actin. The following primers were used: *Actb*, GGCTGTATTCCCCTCCATCG (forward) and CCAGTTGGTAACAATGCCATGT (reverse); *Il17a*, CTCCAGAAGGCCCTCAGACTAC (forward) and AGCTTTCCCTCCGCATTGACACAG (reverse); *Il17f*, GAGGATAACACTGTGAGAGTTGAC (forward) and GAGTTCATGGTGCTGTCTTCC (reverse); *Rorc*, CCGCTGAGAGGGCTTCAC (forward) and TGCAGGAGTAGGCCACATTACA (reverse); *Il21*, ATCCTGAACTTCTATCAGCTCCAC (forward) and GCATTTAGCTATGTGCTTCTGTTTC (reverse); *Il22*, CATGCAGGAGGTGGTACCTT (forward) and CAGACGCAAGCATTTCTCAG (reverse); *Irf4*, TCTTCAAGGCTTGGGCATTG (forward) and CACATCGTAATCTTGTCTTCCAAGTAG (reverse); *Batf*, GTTCTGTTTCTCCAGGTCC (forward) and GAAGAATCGCATCGCTGC (reverse); *Tnfa*, TCCCAGGTTCTCTTCAAGGGA (forward) and GGTGAGGAGCACGTAGTCGG (reverse); *Nfkb2*, CGTTCATAAACAGTATGCCATTGTG (forward) and CCCACGCTTGCGTTTCAG (reverse); *Il10*, GCTCTTACTGACTGGCATGAG (forward) and CGCAGCTCTAGGAGCATGTG (reverse); *Maf*, AGCAGTTGGTGACCATGTCG (forward) and TGGAGATCTCCTGCTTGAGG (reverse); *Nrp1*, ACAAATGTGGCGGGACCATA (forward) and TGGATTAGCCATTCACACTTCTC (reverse); *Pdcd1*, ACCCTGGTCATTCACTTGGG (forward) and CATTTGCTCCCTCTGACACTG (reverse); *Btla*, TGCTTGGGACTCCTCGGTTAT (forward) and ACACAGATTGTTCCATTGTGCT (reverse); *Lag3*, CTGGGACTGCTTTGGGAAG (forward) and GGTTGATGTTGCCAGATAACCC (reverse).

Chromatin immunoprecipitation

At least 5×10^6 cells were used per chromatin immunoprecipitation (ChIP) using the CST SimpleChIP kit (CST #9003) and following the manufacturer's protocol. Anti-RORγt (clone H-190; Santa Cruz Biotechnology #Sc-28559x) was used at 2 μg per ChIP, and rabbit isotype immunoglobulin G control (provided with CST SimpleChIP kit) was used at the same concentration. The following primers were used to amplify RORγt-bound DNA at Btla gene: −49 site: CACCAGGTCTCCTGATTTGA (forward) and AGGAGTCCCAAGCATGGCA (reverse); −369 site, GGTTGTAAGATACATTACACTG (forward) and TCTAAATTGTTACAGTCTTTAGG (reverse). The following primers were used to amplify RORγt-bound DNA at Il17a gene promoter: CTGAAGAGCTGGGACCTAATG (forward) and GCTCTCTCATGTTCTCTCCTCTC (reverse); CNS-5 site, CCGTTTAGACTTGAAACCCAGTC (forward) and GTACCTATGTGTTAGGAGGCGC (reverse).

Microarray gene expression analysis

Sample preparation for microarray hybridization was carried out as described in the NuGEN Ovation PicoSL WTA System V2 and NuGEN Encore Biotin Module manuals (NuGEN Technologies Inc., San Carlos, CA, USA). Briefly, 20 ng of total RNA was reverse-transcribed into double-stranded cDNA in a two-step process, introducing a SPIA tag sequence. Bead-purified cDNA was amplified by a SPIA amplification reaction, followed by an additional bead purification. Four micrograms of SPIA cDNA was fragmented, terminally biotin-labeled, and hybridized to Affymetrix Mouse Gene 2.0 ST arrays for 16 hours at 45°C in a GeneChip Hybridization Oven 640. Hybridized arrays were washed and stained in an Affymetrix Fluidics Station FS450, and the fluorescent signals were measured with an Affymetrix GeneChip Scanner 3000 7G. Fluidics and scan functions were controlled by the Affymetrix GeneChip Command Console v4.1.3 software. Sample processing was performed at an Affymetrix Service Provider and Core Facility, "KFB—Center of Excellence for Fluorescent Bioanalytics" (Regensburg, Germany; www.kfb-regensburg.de). Raw CEL files were normalized using robust multi-array average algorithm from "affy" R package (https://bioconductor.org/packages/release/bioc/html/affy.html) and annotated using pd.mogene.2.0.st from "Oligo" R package (https://bioconductor.org/packages/release/bioc/html/oligo.html). Student's t test P values, adjusted P values (BH test), and $\log_2$ fold changes were calculated using "EMA" R package (https://cran.r-project.org/web/packages/EMA/index.html). Probes that were not annotated with National Center for Biotechnology Information gene ID or annotated as predicted genes were not included in subsequent analysis.

Induction of EAE

EAE was induced by subcutaneous injection of 50 μg of MOG35-55 peptide in CFA, whereas 2 ng of pertussis toxin was intraperitoneally injected on the day of immunization and 2 days later. On the day of immunization, SM at 224 μg per mouse or DMSO was administered by intraperitoneal injection, whereas 1 and 2 days later, either SM was administered at 112 μg per mouse or DMSO was administered as vehicle control.

Proteomics analysis

Cell pellets were lysed in 50 μl of lysis buffer [8 M urea, 75 mM NaCl, 50 mM tris (pH 8.0), and 1 mM EDTA, containing protease and phosphatase inhibitors] on ice for 15 min. Lysates were centrifuged for 10 min at 4°C at 20,000*g* before protein concentrations were determined by bicinchoninic acid assay. The total input from each experimental condition was determined by the limiting reagent, which was 96 μg of protein. Whole-cell lysates were reduced with 5 mM dithiothreitol for 45 min, followed by cysteine alkylation with 10 mM iodoacetamide for 45 min in the dark. Samples were diluted to 2 M urea with 50 mM tris (pH 8.0) and digested with LysC (1:50 enzyme/substrate ratio) for 2 hours at 25°C. Trypsin was then added at the same ratio and digested overnight at 25°C. Formic acid was added to a final concentration of 1%, desalted, and stored at −80°C until tandem mass tag (TMT; Thermo Fisher Scientific lot no. QL228730A) peptide labeling according to manufacturer instructions.

Desalted 10-plex TMT-labeled peptides were subjected to basic reversed-phase (RP) chromatography. Peptides were separated using a 2.1 mm by 250 mm RP Zorbax 300 A Extend-C18 column (3.5-μm bead size; Agilent Technologies) on an Agilent 1100 Series HPLC. The 90-min gradient of solvent A [2% acetonitrile (ACN) and 5 mM ammonium formate (pH 10)] to solvent B [90% ACN and 5 mM ammonium formate (pH 10)] went from 0 to 6% B over 4 min, from 6 to 28.5% B over 50 min, from 28.5 to 34% B over 5.5 min, and from 34 to 60% B over 13 min, ending with an 8.5-min hold at 60% B. The flow rate was 200 nl/min. Eighty-four fractions were collected and concatenated down to 24 final fractions. Five percent of each final fraction was used for proteome analysis.

Proteome analysis was performed using a Proxeon EASY-nLC 1200 UHPLC coupled to an Orbitrap Q Exactive Plus mass spectrometer (Thermo Fisher Scientific). The online peptide separation was performed using a 20 cm by 75 μm (inner diameter) silica picofrit capillary column (New Objectives) packed with 1.9-μm ReproSil-Pur C18-AQ beads (Dr. Maisch GmbH) at 50°C. The 110-min method, 84-min effective gradient of solvent A (3% ACN and 0.1% formic acid) to solvent B (90% ACN and 0.1% formic acid) started at 2% B and went from 2 to 6% B over 1 min, from 6 to 30% B over 85 min, from 30 to 60% B over 9 min, from 60 to 90% B over 1 min, holding for 5 min, ramping down to 50% B over 1 min, and holding for 10 min. The flow rate was 200 nl/min. The Q Exactive Plus mass spectrometer performed data-dependent acquisition in positive ion mode. MS1 spectra scanned a range of 300 to 2000 mass/charge ratio (m/z) at a resolution of 70,000, with a maximum injection time (max IT) of 10 ms for a 3e6 AGC target. The top 12 most abundant peaks, charge state $2 < x < 7$, were selected for MS2 with an isolation width of 1.7 m/z and an offset of 0.3 m/z. The AGC target was set to 5e4 with a max IT of 120 ms. An empirically determined normalized collision energy was set to 31. Dynamic exclusion was set to 15 s.

All .raw files were searched using Spectrum Mill (Agilent Technologies). MS2 spectra were searched against the UniProt Mouse database (20141017, 41,309 mouse entries, 150 common laboratory contaminants), with a mass tolerance of 20 ppm for both the precursor and product ions. The enzyme specificity was set for trypsin, allowing up to three missed cleavages. The fixed modification was carbamidomethylation at cysteine. TMT labeling was required at lysine, but peptide N termini were allowed to be either labeled or unlabeled. To reduce TMT compression, all peptide spectral matches with an MS1 purity of less than 50% were excluded. Allowed variable modifications for whole proteome datasets were acetylation of protein N termini, oxidized methionine, deamidation of asparagine, and pyroglutamic acid at peptide N-terminal glutamine, with a precursor MH+ shift range of −18 to 64 Da. The false discovery rate was less than 1%. For proteome interpretation, protein identifications were discarded if the protein was only observed by a single peptide. For reporting the number of proteins, identified protein subgroups, protein gene products (proteoforms) from the same gene, were expanded to account for the observation of different proteoforms. For statistical tests, protein subgroups were collapsed to the proteoform with the most evidence.

Detection of transcriptional regulatory network

The KCRI network was downloaded as a Cytoscape file from http://th17.bio.nyu.edu/pages/cytoscape.html (16 August 2019) (*6*), and the edges were exported as a tsv file for processing by a custom python script. To select a subset of regulatory genes from the KCRI network, we checked which genes were annotated as targeting the 100 most differentially expressed genes in our dataset. We began with a core set that included all genes annotated as regulating at least 1 of the top 100 genes and which were themselves differentially expressed by at least 45% (*Irf5*, *Trerf1*, *Lef1*, *Myb*, *Aff3*, *Nr4a3*, *Egr3*, *Ar*, *Plxnc1*, *Gata3*, *Plxnd1*, *Nfkb2*, *Batf3*, *Sema4a*, *Lgr4*, *Maf*, *Inhba*, *Nfil3*, *Tiparp*, *Ahr*, *Fosl2*, and *Ssh2*). Visualizing the network of interactions among these genes revealed two modules, which were extended to other genes showing interactions coherent with these modules and selected downstream genes. Ranking genes by annotated targets*differential expression, the two modules include all the top 10 genes and 23 of the top 30.

Model of regulation by the KCRI network

To test whether KCRI annotations could explain our observed gene changes, we predicted a fold change for each of our observed genes. For each gene, we calculated a score by summing the fold change of genes annotated as its regulators multiplied by the KCRI confidence in the interaction. We normalized this score so that the 95 percentile range was identical to the 95 percentile range of observed fold changes and used this normalized score as a predicted fold change. For calculation of the ROC, we compared the sign of the predicted fold changes to the sign of the observed fold changes and calculated true positives and false positives.

Visualization of changes in the proteome

The file 10090.protein.links.v10.5.txt containing interactions for the mouse proteome and 10090.protein.aliases.v10.5.txt containing mappings of gene symbols to the STRING database were downloaded from the STRING website (https://string-db.org/cgi/download.pl?species_text=Mus+musculus; 5 June 2018) (*62*). The interactions are in the form of scores between 0 and 1000 for each protein-protein pair, summarizing all the total strength of evidence. Proteins that were changed by twofold or more comparisons of samples at 0, 24, and 48 hours or in comparisons of DMSO versus SM at 24 and 48 hours,

together with any of the 100 most differentially expressed genes that were not in this set, were selected for analysis. This resulted in a set of 3452 proteins. Of these, 3418 were successfully mapped to STRING using the alias file (unmapped gene symbols: AF357399, Pdcd11, Igf2, 42622, Rpl7, Sapcd2, Rnaseh1, Kctd12, Gins1, Timm13, Lin9, Kansl1, Rpl18, ptplad1, Trac, Ak6, Slc25a22, Hmga2-ps1, Pet117, 42628, Bin2, Scnm1, Chordc1, Adgre5, AB010352, Ecd, Prdx5, Snora36b, 42614, Polr1c, 42431, Dnmt1, Mturn, and Ighm).

tSNE and spectral clustering were carried out in a custom python script using the packages and TSNE and SpectralClustering from scikit-learn. For mapping to tSNE, these were mapped to distances by subtracting the STRING score from 1000, whereas for spectral clustering, scores were used directly as affinities. For spectral clustering to highlight functional protein sets, the number of clusters was set to 8, resulting in seven functional groups and a residual background cluster. On manual examination, the clusters were named examination of the gene lists and pathway analysis in the STRING database. Two clusters were merged, and one outlier group was excluded on the basis of biological significance. For visualizing changes in the proteome, tSNE coordinates derived from the total set of 3452 proteins were used, but only changes that were present in both biological replicates were plotted on the color scale.

Radial autocorrelation

To test for clustering, pairs on points on the tSNE plot were binned by separation, and the autocorrelation at distance r was calculated as the average product of fold changes for the pairs of proteins in bin r divided by the variance of all proteins showing significant change. Smooth fits of exponentials allowing free parameters for amplitude and decay length were carried out. P values were derived from random permutations of the data 1000 times in each comparison, with the null hypothesis that the exponential fit should have amplitude and decay length as long as that in the observed data. Scripts to generate Figs. 2 (D and E) and 3 (A to E) and fig. S3 (C to F) will be made available online.

Statistical analysis

Statistical analyses of transcriptional and proteomic data are described above. All other statistical analyses were performed using GraphPad Prism 7.0. Paired t tests were used to calculate P values when comparing mean fluorescence intensities to account for machine settings and time variability. Paired t tests were used to calculate P values when comparing retroviral infections due to high technical variability between experiments. All other P values were calculated using nonparametric Mann-Whitney test, whereas EAE clinical data were assessed by two-way analysis of variance (ANOVA) and Bonferroni's multiple comparisons test, and densitometry was analyzed by one-way ANOVA and Fisher's least significant difference (LSD) test.

SUPPLEMENTARY MATERIALS

stke.sciencemag.org/cgi/content/full/12/596/eaaw3469/DC1

Fig. S1. SMs do not prevent activation and proliferation of T_H17 cells.

Fig. S2. SMs promote NIK-dependent production of TNF in T_H17 cells.

Fig. S3. SMs do not alter RORγt, IRF4, or BATF protein amounts in T_H17 cells.

Fig. S4. Single cIAP deficiency cannot recapitulate SM-induced inhibition of T_H17 cell differentiation.

Fig. S5. Proteomic changes in T_H17 cells compared to undifferentiated $CD4^+$ T cells.

Fig. S6. SMs induce global transcriptional and proteomic changes in T_H17 cells.

Fig. S7. Reduced abundance of metabolic proteins in T_H17 compared to undifferentiated $CD4^+$ T cells.

Fig. S8. SM increases the abundance of noncanonical NF-κB and cell adhesion proteins in T_H17 cells.

Fig. S9. RelB induces the expression of *Nfkb2* and reduces the expression of *Il17a* independently of p52.

Fig. S10. SM treatment hinders RORγt binding to *Il17a* regulatory regions and increases the expression of immune checkpoint receptors in T_H17 cells.

Fig. S11. SM depletion of cIAP1 but not xIAP activates the noncanonical NF-κB and does not alter the nuclear translocation of T_H17-associated TFs.

Data file S1. Differentially expressed genes in DMSO- versus SM-treated T_H17 cells.

Data file S2. Differentially expressed proteins in DMSO- versus SM-treated T_H17 cells.

Data file S3. Proteins and pathways differentially regulated in T_H17 compared to undifferentiated cells.

Data file S4. Proteins and pathways differentially regulated in DMSO- and SM-treated T_H17 cells.

REFERENCES AND NOTES

1. C. Schiering, E. Wincent, A. Metidji, A. Iseppon, Y. Li, A. J. Potocnik, S. Omenetti, C. J. Henderson, C. R. Wolf, D. W. Nebert, B. Stockinger, Feedback control of AHR signalling regulates intestinal immunity. *Nature* **542**, 242–245 (2017).
2. H. R. Conti, F. Shen, N. Nayyar, E. Stocum, J. N. Sun, M. J. Lindemann, A. W. Ho, J. H. Hai, J. J. Yu, J. W. Jung, S. G. Filler, P. Masso-Welch, M. Edgerton, S. L. Gaffen, Th17 cells and IL-17 receptor signaling are essential for mucosal host defense against oral candidiasis. *J. Exp. Med.* **206**, 299–311 (2009).
3. I. I. Ivanov, B. S. McKenzie, L. Zhou, C. E. Tadokoro, A. Lepelley, J. J. Lafaille, D. J. Cua, D. R. Littman, The orphan nuclear receptor RORγt directs the differentiation program of proinflammatory IL-17$^+$ T helper cells. *Cell* **126**, 1121–1133 (2006).
4. M. Noack, P. Miossec, Th17 and regulatory T cell balance in autoimmune and inflammatory diseases. *Autoimmun. Rev.* **13**, 668–677 (2014).
5. J. Zhu, H. Yamane, W. E. Paul, Differentiation of effector CD4 T cell populations. *Annu. Rev. Immunol.* **28**, 445–489 (2010).
6. M. Ciofani, A. Madar, C. Galan, M. L. Sellars, K. Mace, F. Pauli, A. Agarwal, W. Huang, C. N. Parkurst, M. Muratet, K. M. Newberry, S. Meadows, A. Greenfield, Y. Yang, P. Jain, F. K. Kirigin, C. Birchmeier, E. F. Wagner, K. M. Murphy, R. M. Myers, R. Bonneau, D. R. Littman, A validated regulatory network for Th17 cell specification. *Cell* **151**, 289–303 (2012).
7. A. Brüstle, S. Heink, M. Huber, C. Rosenplänter, C. Stadelmann, P. Yu, E. Arpaia, T. W. Mak, T. Kamradt, M. Lohoff, The development of inflammatory T_H-17 cells requires interferon-regulatory factor 4. *Nat. Immunol.* **8**, 958–966 (2007).
8. B. U. Schraml, K. Hildner, W. Ise, W.-L. Lee, W. A.-E. Smith, B. Solomon, G. Sahota, J. Sim, R. Mukasa, S. Cemerski, R. D. Hatton, G. D. Stormo, C. T. Weaver, J. H. Russell, T. L. Murphy, K. M. Murphy, The AP-1 transcription factor *Batf* controls T_H17 differentiation. *Nature* **460**, 405–409 (2009).
9. P. Li, R. Spolski, W. Liao, L. Wang, T. L. Murphy, K. M. Murphy, W. J. Leonard, BATF–JUN is critical for IRF4-mediated transcription in T cells. *Nature* **490**, 543–546 (2012).
10. E. Glasmacher, S. Agrawal, A. B. Chang, T. L. Murphy, W. Zeng, B. Vander Lugt, A. A. Khan, M. Ciofani, C. J. Spooner, S. Rutz, J. Hackney, R. Nurieva, C. R. Escalante, W. Ouyang, D. R. Littman, K. M. Murphy, H. Singh, A genomic regulatory element that directs assembly and function of immune-specific AP-1–IRF complexes. *Science* **338**, 975–980 (2012).
11. A. T. Bauquet, H. Jin, A. M. Paterson, M. Mitsdoerffer, I.-C. Ho, A. H. Sharpe, V. K. Kuchroo, The costimulatory molecule ICOS regulates the expression of c-Maf and IL-21 in the development of follicular T helper cells and T_H-17 cells. *Nat. Immunol.* **10**, 167–175 (2009).
12. X. O. Yang, A. D. Panopoulos, R. Nurieva, S. H. Chang, D. Wang, S. S. Watowich, C. Dong, STAT3 regulates cytokine-mediated generation of inflammatory helper T cells. *J. Biol. Chem.* **282**, 9358–9363 (2007).
13. S. Gerondakis, T. S. Fulford, N. L. Messina, R. J. Grumont, NF-κB control of T cell development. *Nat. Immunol.* **15**, 15–25 (2014).
14. H. Oh, S. Ghosh, NF-κB: Roles and regulation in different CD4$^+$ T-cell subsets. *Immunol. Rev.* **252**, 41–51 (2013).
15. J. Napetschnig, H. Wu, Molecular basis of NF-κB signaling. *Annu. Rev. Biophys.* **42**, 443–468 (2013).
16. J. Ruland, Return to homeostasis: Downregulation of NF-κB responses. *Nat. Immunol.* **12**, 709–714 (2011).
17. Q. Ruan, V. Kameswaran, Y. Zhang, S. Zheng, J. Sun, J. Wang, J. DeVirgiliis, H.-C. Liou, A. A. Beg, Y. H. Chen, The Th17 immune response is controlled by the Rel–RORγ–RORγT transcriptional axis. *J. Exp. Med.* **208**, 2321–2333 (2011).
18. X. Xiao, X. Shi, Y. Fan, C. Wu, X. Zhang, L. Minze, W. Liu, R. M. Ghobrial, P. Lan, X. C. Li, The costimulatory receptor OX40 inhibits interleukin-17 expression through activation of repressive chromatin remodeling pathways. *Immunity* **44**, 1271–1283 (2016).
19. X. Xiao, S. Balasubramanian, W. Liu, X. Chu, H. Wang, E. J. Taparowsky, Y.-X. Fu, Y. Choi, M. C. Walsh, X. C. Li, OX40 signaling favors the induction of T_H9 cells and airway inflammation. *Nat. Immunol.* **13**, 981–990 (2012).
20. M. Gyrd-Hansen, P. Meier, IAPs: From caspase inhibitors to modulators of NF-κB, inflammation and cancer. *Nat. Rev. Cancer* **10**, 561–574 (2010).
21. A. Annibaldi, S. Wicky John, T. Vanden Berghe, K. N. Swatek, J. Ruan, G. Liccardi, K. Bianchi, P. R. Elliott, S. M. Choi, S. Van Coillie, J. Bertin, H. Wu, D. Komander, P. Vandenabeele,

J. Silke, P. Meier, Ubiquitin-mediated regulation of RIPK1 kinase activity independent of IKK and MK2. *Mol. Cell* **69**, 566–580.e5 (2018).
22. O. Micheau, J. Tschopp, Induction of TNF receptor I-mediated apoptosis via two sequential signaling complexes. *Cell* **114**, 181–190 (2003).
23. S. Vallabhapurapu, A. Matsuzawa, W. Zhang, P.-H. Tseng, J. J. Keats, H. Wang, D. A. A. Vignali, P. L. Bergsagel, M. Karin, Nonredundant and complementary functions of TRAF2 and TRAF3 in a ubiquitination cascade that activates NIK-dependent alternative NF-κB signaling. *Nat. Immunol.* **9**, 1364–1370 (2008).
24. B. J. Zarnegar, Y. Wang, D. J. Mahoney, P. W. Dempsey, H. H. Cheung, J. He, T. Shiba, X. Yang, W.-c. Yeh, T. W. Mak, R. G. Korneluk, G. Cheng, Noncanonical NF-κB activation requires coordinated assembly of a regulatory complex of the adaptors cIAP1, cIAP2, TRAF2 and TRAF3 and the kinase NIK. *Nat. Immunol.* **9**, 1371–1378 (2008).
25. H. Sanjo, D. M. Zajonc, R. Braden, P. S. Norris, C. F. Ware, Allosteric regulation of the ubiquitin:NIK and ubiquitin:TRAF3 E3 ligases by the lymphotoxin-β receptor. *J. Biol. Chem.* **285**, 17148–17155 (2010).
26. S.-C. Sun, The non-canonical NF-κB pathway in immunity and inflammation. *Nat. Rev. Immunol.* **17**, 545–558 (2017).
27. C. Du, M. Fang, Y. Li, L. Li, X. Wang, Smac, a mitochondrial protein that promotes cytochrome c–dependent caspase activation by eliminating IAP inhibition. *Cell* **102**, 33–42 (2000).
28. A. M. Verhagen, P. G. Ekert, M. Pakusch, J. Silke, L. M. Connolly, G. E. Reid, R. L. Moritz, R. J. Simpson, D. L. Vaux, Identification of DIABLO, a mammalian protein that promotes apoptosis by binding to and antagonizing IAP proteins. *Cell* **102**, 43–53 (2000).
29. J. E. Vince, W. W.-L. Wong, N. Khan, R. Feltham, D. Chau, A. U. Ahmed, C. A. Benetatos, S. K. Chunduru, S. M. Condon, M. McKinlay, R. Brink, M. Leverkus, V. Tergaonkar, P. Schneider, B. A. Callus, F. Koentgen, D. L. Vaux, J. Silke, IAP antagonists target cIAP1 to induce TNFα-dependent apoptosis. *Cell* **131**, 682–693 (2007).
30. E. Varfolomeev, J. W. Blankenship, S. M. Wayson, A. V. Fedorova, N. Kayagaki, P. Garg, K. Zobel, J. N. Dynek, L. O. Elliott, H. J. A. Wallweber, J. A. Flygare, W. J. Fairbrother, K. Deshayes, V. M. Dixit, D. Vucic, IAP antagonists induce autoubiquitination of c-IAPs, NF-κB activation, and TNFα-dependent apoptosis. *Cell* **131**, 669–681 (2007).
31. S. T. Beug, H. H. Cheung, T. Sanda, M. St-Jean, C. E. Beauregard, H. Mamady, S. D. Baird, E. C. LaCasse, R. G. Korneluk, The transcription factor SP3 drives TNF-α expression in response to Smac mimetics. *Sci. Signal.* **12**, eaat9563 (2019).
32. G. Brumatti, C. Ma, N. Lalaoui, N.-Y. Nguyen, M. Navarro, M. C. Tanzer, J. Richmond, M. Ghisi, J. M. Salmon, N. Silke, G. Pomilio, S. P. Glaser, E. de Valle, R. Gugasyan, M. A. Gurthridge, S. M. Condon, R. W. Johnstone, R. Lock, G. Salvesen, A. Wei, D. L. Vaux, P. G. Ekert, J. Silke, The caspase-8 inhibitor emricasan combines with the SMAC mimetic birinapant to induce necroptosis and treat acute myeloid leukemia. *Sci. Transl. Med.* **8**, 339ra69 (2016).
33. S. McComb, J. Aguadé-Gorgorió, L. Harder, B. Marovca, G. Cario, C. Eckert, M. Schrappe, M. Stanulla, A. von Stackelberg, J.-P. Bourquin, B. C. Bornhauser, Activation of concurrent apoptosis and necroptosis by SMAC mimetics for the treatment of refractory and relapsed ALL. *Sci. Transl. Med.* **8**, 339ra70 (2016).
34. S. T. Beug, C. E. Beauregard, C. Healy, T. Sanda, M. St-Jean, J. Chabot, D. E. Walker, A. Mohan, N. Earl, X. Lun, D. L. Senger, S. M. Robbins, P. Staeheli, P. A. Forsyth, T. Alain, E. C. LaCasse, R. G. Korneluk, Smac mimetics synergize with immune checkpoint inhibitors to promote tumour immunity against glioblastoma. *Nat. Commun.* **8**, 14278 (2017).
35. C. J. Kearney, N. Lalaoui, A. J. Freeman, K. M. Ramsbottom, J. Silke, J. Oliaro, PD-L1 and IAPs co-operate to protect tumors from cytotoxic lymphocyte-derived TNF. *Cell Death Differ.* **24**, 1705–1716 (2017).
36. M. Dougan, S. Dougan, J. Slisz, B. Firestone, M. Vanneman, D. Draganov, G. Goyal, W. Li, D. Neuberg, R. Blumberg, N. Hacohen, D. Porter, L. Zawel, G. Dranoff, IAP inhibitors enhance co-stimulation to promote tumor immunity. *J. Exp. Med.* **207**, 2195–2206 (2010).
37. E. Clancy-Thompson, L. Ali, P. T. Bruck, M. A. Exley, R. S. Blumberg, G. Dranoff, M. Dougan, S. K. Dougan, IAP antagonists enhance cytokine production from mouse and human iNKT cells. *Cancer Immunol. Res.* **6**, 25–35 (2018).
38. G. R. Campbell, R. S. Bruckman, Y.-L. Chu, R. N. Trout, S. A. Spector, SMAC mimetics induce autophagy-dependent apoptosis of HIV-1-infected resting memory CD4+ T cells. *Cell Host Microbe* **24**, 689–702.e7 (2018).
39. D. J. Mahoney, H. H. Cheung, R. L. Mrad, S. Plenchette, C. Simard, E. Enwere, V. Arora, T. W. Mak, E. C. Lacasse, J. Waring, R. G. Korneluk, Both cIAP1 and cIAP2 regulate TNFα-mediated NF-κB activation. *Proc. Natl. Acad. Sci. U.S.A.* **105**, 11778–11783 (2008).
40. N. Yosef, A. K. Shalek, J. T. Gaublomme, H. Jin, Y. Lee, A. Awasthi, C. Wu, K. Karwacz, S. Xiao, M. Jorgolli, D. Gennert, R. Satija, A. Shakya, D. Y. Lu, J. J. Trombetta, M. R. Pillai, P. J. Ratcliffe, M. L. Coleman, M. Bix, D. Tantin, H. Park, V. K. Kuchroo, A. Regev, Dynamic regulatory network controlling T_H17 cell differentiation. *Nature* **496**, 461–468 (2013).
41. L. Z. Shi, R. Wang, G. Huang, P. Vogel, G. Neale, D. R. Green, H. Chi, HIF1α–dependent glycolytic pathway orchestrates a metabolic checkpoint for the differentiation of T_H17 and T_{reg} cells. *J. Exp. Med.* **208**, 1367–1376 (2011).
42. V. A. Gerriets, R. J. Kishton, A. G. Nichols, A. N. Macintyre, M. Inoue, O. Ilkayeva, P. S. Winter, X. Liu, B. Priyadharshini, M. E. Slawinska, L. Haeberli, C. Huck, L. A. Turka, K. C. Wood, L. P. Hale, P. A. Smith, M. A. Schneider, N. J. MacIver, J. W. Locasale, C. B. Newgard, M. L. Shinohara, J. C. Rathmell, Metabolic programming and PDHK1 control $CD4^+$ T cell subsets and inflammation. *J. Clin. Invest.* **125**, 194–207 (2015).
43. L. Sun, J. Fu, Y. Zhou, Metabolism controls the balance of Th17/T-regulatory cells. *Front. Immunol.* **8**, 1632 (2017).
44. T. Siggers, A. B. Chang, A. Teixeira, D. Wong, K. J. Williams, B. Ahmed, J. Ragoussis, I. A. Udalova, S. T. Smale, M. L. Bulyk, Principles of dimer-specific gene regulation revealed by a comprehensive characterization of NF-κB family DNA binding. *Nat. Immunol.* **13**, 95–102 (2011).
45. B. Zhao, L. A. Barrera, I. Ersing, B. Willox, S. C. S. Schmidt, H. Greenfeld, H. Zhou, S. B. Mollo, T. T. Shi, K. Takasaki, S. Jiang, E. Cahir-McFarland, M. Kellis, M. L. Bulyk, E. Kieff, B. E. Gewurz, The NF-κB genomic landscape in lymphoblastoid B cells. *Cell Rep.* **8**, 1595–1606 (2014).
46. V. Bekiaris, J. R. Šedý, M. G. Macauley, A. Rhode-Kurnow, C. F. Ware, The inhibitory receptor BTLA controls γδ T cell homeostasis and inflammatory responses. *Immunity* **39**, 1082–1094 (2013).
47. S. Rutz, R. Noubade, C. Eidenschenk, N. Ota, W. Zeng, Y. Zheng, J. Hackney, J. Ding, H. Singh, W. Ouyang, Transcription factor c-Maf mediates the TGF-β-dependent suppression of IL-22 production in T_H17 cells. *Nat. Immunol.* **12**, 1238–1245 (2011).
48. M. Veldhoen, K. Hirota, A. M. Westendorf, J. Buer, L. Dumoutier, J.-C. Renauld, B. Stockinger, The aryl hydrocarbon receptor links T_H17-cell-mediated autoimmunity to environmental toxins. *Nature* **453**, 106–109 (2008).
49. C. S. Constantinescu, N. Farooqi, K. O'Brien, B. Gran, Experimental autoimmune encephalomyelitis (EAE) as a model for multiple sclerosis (MS). *Br. J. Pharmacol.* **164**, 1079–1106 (2011).
50. V. Brucklacher-Waldert, C. Ferreira, S. Innocentin, S. Kamdar, D. R. Withers, M. C. Kullberg, M. Veldhoen, Tbet or continued RORγt expression is not required for Th17-associated immunopathology. *J. Immunol.* **196**, 4893–4904 (2016).
51. I. Mohammad, K. Nousiainen, S. D. Bhosale, I. Starskaia, R. Moulder, A. Rokka, F. Cheng, P. Mohanasundaram, J. E. Eriksson, D. R. Goodlett, H. Lähdesmäki, Z. Chen, Quantitative proteomic characterization and comparison of T helper 17 and induced regulatory T cells. *PLoS Biol.* **16**, e2004194 (2018).
52. Y. Grinberg-Bleyer, R. Caron, J. J. Seeley, N. S. De Silva, C. W. Schindler, M. S. Hayden, U. Klein, S. Ghosh, The alternative NF-κB pathway in regulatory T cell homeostasis and suppressive function. *J. Immunol.* **200**, 2362–2371 (2018).
53. J.-F. Bach, The effect of infections on susceptibility to autoimmune and allergic diseases. *N. Engl. J. Med.* **347**, 911–920 (2002).
54. C. Ohnmacht, J.-H. Park, S. Cording, J. B. Wing, K. Atarashi, Y. Obata, V. Gaboriau-Routhiau, R. Marques, S. Dulauroy, M. Fedoseeva, M. Busslinger, N. Cerf-Bensussan, I. G. Boneca, D. Voehringer, K. Hase, K. Honda, S. Sakaguchi, G. Eberl, The microbiota regulates type 2 immunity through $ROR\gamma t^+$ T cells. *Science* **349**, 989–993 (2015).
55. C. M. Finlay, K. P. Walsh, K. H. G. Mills, Induction of regulatory cells by helminth parasites: Exploitation for the treatment of inflammatory diseases. *Immunol. Rev.* **259**, 206–230 (2014).
56. G. Eberl, Immunity by equilibrium. *Nat. Rev. Immunol.* **16**, 524–532 (2016).
57. H. D. Brightbill, E. Suto, N. Blaquiere, N. Ramamoorthi, S. Sujatha-Bhaskar, E. B. Gogol, G. M. Castanedo, B. T. Jackson, Y. C. Kwon, S. Haller, J. Lesch, K. Bents, C. Everett, P. B. Kohli, S. Linge, L. Christian, K. Barrett, A. Jaochico, L. M. Berezhkovskiy, P. W. Fan, Z. Modrusan, K. Veliz, M. J. Townsend, J. DeVoss, A. R. Johnson, R. Godemann, W. P. Lee, C. D. Austin, B. S. McKenzie, J. A. Hackney, J. J. Crawford, S. T. Staben, M. H. Alaoui Ismaili, L. C. Wu, N. Ghilardi, NF-κB inducing kinase is a therapeutic target for systemic lupus erythematosus. *Nat. Commun.* **9**, 179 (2018).
58. W. W. Wong, J. E. Vince, N. Lalaoui, K. E. Lawlor, D. Chau, A. Bankovacki, H. Anderton, D. Metcalf, L. O'Reilly, P. J. Jost, J. M. Murphy, W. S. Alexander, A. Strasser, D. L. Vaux, J. Silke, cIAPs and XIAP regulate myelopoiesis through cytokine production in an RIPK1- and RIPK3-dependent manner. *Blood* **123**, 2562–2572 (2014).
59. M. Hahn, A. Macht, A. Waisman, N. Hövelmeyer, NF-κB-inducing kinase is essential for B-cell maintenance in mice. *Eur. J. Immunol.* **46**, 732–741 (2016).
60. M. Lochner, L. Peduto, M. Cherrier, S. Sawa, F. Langa, R. Varona, D. Riethmacher, M. Si-Tahar, J. P. Di Santo, G. Eberl, In vivo equilibrium of proinflammatory $IL\text{-}17^+$ and regulatory $IL\text{-}10^+$ $Foxp3^+$ $ROR\gamma t^+$ T cells. *J. Exp. Med.* **205**, 1381–1393 (2008).
61. C. Neumann, F. Heinrich, K. Neumann, V. Junghans, M.-F. Mashreghi, J. Ahlers, M. Janke, C. Rudolph, N. Mockel-Tenbrinck, A. A. Kühl, M. M. Heimesaat, C. Esser, S.-H. Im, A. Radbruch, S. Rutz, A. Scheffold, Role of Blimp-1 in programing Th effector cells into IL-10 producers. *J. Exp. Med.* **211**, 1807–1819 (2014).
62. D. Szklarczyk, J. H. Morris, H. Cook, M. Kuhn, S. Wyder, M. Simonovic, A. Santos, N. T. Doncheva, A. Roth, P. Bork, L. J. Jensen, C. von Mering, The STRING database in 2017: Quality-controlled protein–protein association networks, made broadly accessible. *Nucleic Acids Res.* **45**, D362–D368 (2017).

Acknowledgments: We thank C. C. Neumann and A. Scheffold (German Rheumatism Research Centre Berlin, Germany) for providing the pMig-cMAF plasmid. We thank G. Eberl (Pasteur Institute, Paris, France) for providing RORγt-GFP mice. **Funding:** This work and V.B. were supported by the Lundbeck Foundation grant R163-2013-15201, and J.R. and R.A. were supported by DTU PhD scholarships. D.K. was supported by the Leo Foundation grant LF16020. W.W.-L.W. was supported by the SNF Project grant 310030_159613, and A.W. was supported by the Deutsche Forschungsgemeinschaft WA1600/10-1. S.A.C. and parts of this work were also supported by National Cancer Institute (NCI) Clinical Proteomic Tumor Analysis Consortium grants NIH/NCI U24-CA210986 and NIH/NCI U01 CA214125. **Author contributions:** V.B. designed the study, oversaw the work, performed experiments, and wrote the manuscript. J.R. designed and performed experiments, analyzed data, and helped in writing the manuscript. J.K. designed data analysis pipelines, analyzed the data, and helped in writing the manuscript. R.A., D.K., S.A.M., M.J.S., and S.A.C. contributed with experiments and data analysis. F.I. and W.W.A. contributed with experiments and provided lab space. W.W.-L.W. and A.W. provided materials and contributed to experimental design. **Competing interests:** The authors declare that they have no competing interests. **Data and materials availability.** The microarray data have been deposited in the ArrayExpress repository with the dataset identifier E-MTAB-7894. The mass spectrometry proteomics data have been deposited in the MassIVE repository with the dataset identifier MSV000082955. The IAP knockout mice required a material transfer agreement from the Walter and Eliza Hall Institute of Medical Research. The RORγt-GFP reporter mice required a material transfer agreement from the Pasteur Institute de Paris. All other data needed to evaluate the conclusions in the paper are present in the paper or the Supplementary Materials.

Submitted 11 December 2018
Accepted 7 August 2019
Published 27 August 2019
10.1126/scisignal.aaw3469

Citation: J. Rizk, J. Kaplinsky, R. Agerholm, D. Kadekar, F. Ivars, W. W. Agace, W. W.-L. Wong, M. J. Szucs, S. A. Myers, S. A. Carr, A. Waisman, V. Bekiaris, SMAC mimetics promote NIK-dependent inhibition of $CD4^+$ T_H17 cell differentiation. *Sci. Signal.* **12**, eaaw3469 (2019).

Science Signaling

SMAC mimetics promote NIK-dependent inhibition of CD4$^+$ T_H17 cell differentiation

John Rizk, Joseph Kaplinsky, Rasmus Agerholm, Darshana Kadekar, Fredrik Ivars, William W. Agace, W. Wei-Lynn Wong, Matthew J. Szucs, Samuel A. Myers, Steven A. Carr, Ari Waisman and Vasileios Bekiaris

Sci. Signal. **12** (596), eaaw3469.
DOI: 10.1126/scisignal.aaw3469

SMACing down T_H17 cells

Currently in clinical trials for cancer therapy, second mitochondria-derived activator of caspase (SMAC) mimetics (SMs) target inhibitor of apoptosis proteins (IAPs) for degradation and sensitize tumors to tumor necrosis factor–α (TNF-α)–dependent cell death (see the Focus by Dougan and Dougan). In addition, SMs synergize with immune checkpoint inhibitors to promote durable tumor immunity in mice. Using a multiomics approach, Rizk *et al.* found that SMs altered CD4$^+$ T helper (T_H) cell differentiation. In vitro, SMs reduced T_H17 cell differentiation in an NF-κB–inducing kinase (NIK)–dependent manner and increased the differentiation of T_H9 and T_H2 cells producing IL-9 and IL-13. SMs reduced the production of IL-17 and disease severity in a mouse model of multiple sclerosis. This study defines how these targeted agents alter T cell function and suggests that they may have therapeutic activity in T_H17 cell–driven autoimmune diseases.